

DISSOLUTION AND SURFACE PROXIMITY EFFECTS OF LOW ENERGY,  
AMORPHIZING GERMANIUM IMPLANTS INTO SILICON

By

ANDREW C. KING

A THESIS PRESENTED TO THE GRADUATE SCHOOL  
OF THE UNIVERSITY OF FLORIDA IN PARTIAL FULFILLMENT  
OF THE REQUIREMENTS FOR THE DEGREE OF  
MASTER OF SCIENCE

UNIVERSITY OF FLORIDA

2003

Copyright 2003

by

Andrew C. King

For Mom, Dad and Devin

## ACKNOWLEDGMENTS

I would first like to thank my advisor, Dr. Kevin Jones, for his guidance, patience, commitment to science, and sense of humor. I would also like to thank Dr. Mark Law for answering all of my questions and giving me excellent suggestions throughout my research. Appreciation is also given to Dr. David Norton for support on my committee. I am sincerely grateful to Mark Clark, Tony Saavedra, Andres Gutierrez, Russ Robison, Ljubo Radic, and Carrie Ross for taking time to help me. Without their help I would not have been able to complete this work. Finally, I would like to thank everybody in the SWAMP Group for their friendship and support. The Semiconductor Research Corporation supported this work.

## TABLE OF CONTENTS

	<u>Page</u>
ACKNOWLEDGMENTS .....	iv
LIST OF TABLES .....	vii
LIST OF FIGURES.....	viii
ABSTRACT .....	xi
CHAPTER	
1 INTRODUCTION.....	1
1.1 Background and Motivation .....	1
1.2 Ion Implantation .....	4
1.3 Solid Phase Epitaxy .....	8
1.4 End-of-Range Damage .....	9
1.4.1 Defect Evolution.....	10
1.4.2 Transient Enhanced Diffusion.....	12
1.5 Effect of the Free Surface on End-of-Range Damage.....	14
1.6 Scope and Approach of this Study .....	16
2 EXPERIMENTAL AND DATA EXTRACTION PROCEDURES.....	18
2.1 Transmission Electron Microscopy .....	18
2.1.1 Plan-view Transmission Electron Microscopy Sample Preparation .....	19
2.1.2 Cross-Section Transmission Electron Microscopy Sample Preparation ...	20
2.1.3 Extraction of Defect Parameters from PTEM.....	22
2.1.3.1 Extraction of defect densities from PTEM.....	22
2.1.3.2 Extraction of trapped interstitial concentrations from PTEM.....	23
2.2 Variable Angle Spectroscopic Ellipsometry .....	24
2.3 UT – Marlowe .....	25
2.4 5 keV Ge <sup>+</sup> Defect Dissolution Study.....	26
2.4.1 5 keV Defect Dissolution Activation Energy Experiment.....	27
2.4.2 Surface Lapping Experiment.....	28
2.6 Surface Proximity Experiment.....	29
2.7 Ellipsometry Experiment .....	30

3	5 keV Ge <sup>+</sup> DEFECT DISSOLUTION STUDY.....	31
3.1	Overview.....	31
3.2	Defect Dissolution Activation Energy.....	32
3.2.1	TEM Results.....	32
3.2.2	Extraction of Defect Dissolution Activation Energy.....	34
3.3	Surface Lapping Experiment .....	35
3.3.1	Amorphous Layer Lapping Results.....	35
3.3.2	Defect Evolution.....	36
3.4	UT-Marlowe Simulations .....	36
3.4.1	Simulation Results.....	37
3.4.2	NEI calculation.....	37
3.5	Discussion.....	38
3.6	Conclusion .....	39
4	SURFACE PROXIMITY EXPERIMENT.....	60
4.1	Overview.....	60
4.2	Experimental Results.....	60
4.3	Discussion.....	62
4.4	Conclusion .....	63
5	LOW TEMPERATURE ANNEAL EFFECT ON ELLIPSOMETRY ACCURACY FOR SHALLOW AMORPHOUS SILICON LAYERS .....	75
5.1	Overview.....	75
5.2	Experimental Results.....	75
5.3	Conclusion .....	76
6	CONCLUSIONS AND FUTURE WORK.....	83
6.1	5 keV Ge <sup>+</sup> Defect Dissolution Study.....	83
6.2	Surface Proximity Experiment.....	84
6.3	Low Temperature Anneal Effect on Ellipsometry Accuracy for Shallow Amorphous Silicon Layers .....	85
6.4	Implications of Findings.....	85
	LIST OF REFERENCES .....	87
	BIOGRAPHICAL SKETCH.....	91

## LIST OF TABLES

<u>Table</u>	<u>page</u>
1.1 2002 ITRS doping technology requirements .....	4
3.1 Time range where defect dissolution occurs at each annealing temperature as observed by PTEM. ....	33
3.2 Ellipsometry measurements of amorphous layer thickness for the 5, 10, and 10 keV lapped specimens. ....	36

## LIST OF FIGURES

<u>Figure</u>	<u>page</u>
1.1 Cross-sectional schematic of a MOSFET.....	3
1.2 EOR damage created from an amorphizing implant .....	10
1.3 Defect evolution of excess interstitials resulting from ion implantation into silicon and subsequent annealing .....	11
1.4 Defect evolution reported by Gutierrez for Ge <sup>+</sup> implanted at energies of 5, 10, and 30 keV at a constant dose of 10 <sup>15</sup> cm <sup>-2</sup> annealed at 750 °C.....	13
3.2 PTEM micrographs of 5 keV Ge <sup>+</sup> , 1 x 10 <sup>15</sup> cm <sup>-2</sup> Ge <sup>+</sup> annealed at 725 °C for (a)15 min, (b) 60 min, (c) 65 min, (d) 70 min, and (e) 80 min. ....	40
3.2 PTEM micrographs of 5 keV Ge <sup>+</sup> , 1 x 10 <sup>15</sup> cm <sup>-2</sup> Ge <sup>+</sup> annealed at 750 °C for (a) 5 min, (b) 15 min, (c) 45 min, (d) 60 min, and (e) 65 min. ....	41
3.3 PTEM micrographs of 5 keV Ge <sup>+</sup> , 1 x 10 <sup>15</sup> cm <sup>-2</sup> Ge <sup>+</sup> annealed at 775 °C for (a) 15 min, (b) 35 min, (c) 40 min, and (d) 45 min. ....	42
3.4 PTEM micrographs of 5 keV Ge <sup>+</sup> , 1 x 10 <sup>15</sup> cm <sup>-2</sup> Ge <sup>+</sup> annealed at 825 °C for (a) 15 min, (b) 30 min, and (c) 35 min. ....	43
3.5 PTEM micrographs of 5 keV Ge <sup>+</sup> , 1 x 10 <sup>15</sup> cm <sup>-2</sup> Ge <sup>+</sup> annealed at 875 °C for (a) 5 min, (b) 10 min, and (c) 15 min. ....	44
3.6 PTEM micrograph of 5 keV Ge <sup>+</sup> , 1 x 10 <sup>15</sup> cm <sup>-2</sup> Ge <sup>+</sup> annealed at 775 °C for 35 min imaged at the g <sub>040</sub> condition. ....	45
3.7 Defect density trends for 5 keV, 1x 10 <sup>15</sup> Ge <sup>+</sup> cm <sup>-2</sup> implant over time annealed at 725, 750, 775, 825, and 875 °C.....	46
3.8 Trapped interstitial trends for 5 keV, 1x 10 <sup>15</sup> Ge <sup>+</sup> cm <sup>-2</sup> implant over time annealed at 725, 750, 775, 825, and 875 °C.....	47
3.9 Average defect diameter over time for the 5 keV, 1 x 10 <sup>15</sup> Ge <sup>+</sup> cm <sup>-2</sup> implant annealed at 725, 750, 775, 825, and 875 °C. ....	48

3.10	Defect dissolution rates versus inverse temperature, plotted in Arrhenius form. The trend is show as a least square exponential curve fit.....	49
3.11	High-resolution cross section TEM micrographs of the amorphous layer thickness for (a) 10 keV, (b) 10 keV-lapped, and (c) 5 keV samples.....	50
3.12	PTEM micrographs of the 10 keV Ge <sup>+</sup> , 1 x 10 <sup>15</sup> cm <sup>-2</sup> Ge <sup>+</sup> control implant annealed at 750 °C for (a) 5 min, (b) 15 min, (c) 30 min, (d) 45 min, (e) 60 min, and (f) 360 min.....	51
3.13	PTEM micrographs of the 10 keV Ge <sup>+</sup> , 1 x 10 <sup>15</sup> cm <sup>-2</sup> Ge <sup>+</sup> implant whose amorphous layer was polished to 80 Å and annealed at 750 °C for (a) 5 min, (b) 15 min, (c) 30 min, (d) 45 min, (e) 60 min, and (f) 360 min.....	52
3.14	Defect evolution of the 5 keV, 10 keV, and 10 keV-lapped specimens annealed at 750 °C.....	53
3.15	UT-Marlowe <i>.rbs</i> output for the 5 keV, 1 x 10 <sup>15</sup> Ge <sup>+</sup> cm <sup>-2</sup> implant.....	54
3.16	UT-Marlowe simulated interstitial and vacancy profiles for the 5 keV, 1 x 10 <sup>15</sup> Ge <sup>+</sup> cm <sup>-2</sup> implant. ....	55
3.17	UT-Marlowe <i>.rbs</i> output for the 10 keV, 1 x 10 <sup>15</sup> Ge <sup>+</sup> cm <sup>-2</sup> implant.....	56
3.18	UT-Marlowe simulated interstitial and vacancy profiles for the 10 keV, 1 x 10 <sup>15</sup> Ge <sup>+</sup> cm <sup>-2</sup> implant. ....	57
3.19	NEI profile for the 5 and 10 keV, 1 x 10 <sup>15</sup> Ge <sup>+</sup> cm <sup>-2</sup> implants.....	58
3.20	Trapped interstitial concentrations from 5, 10 and 30 keV, 1 x 10 <sup>15</sup> cm <sup>-2</sup> Ge <sup>+</sup> implants annealed at 750 °C, as reported by Gutierrez. ....	59
4.1	XTEM images of 10 keV 1 x 10 <sup>15</sup> Ge <sup>+</sup> cm <sup>-2</sup> specimens whose amorphous layers were lapped to (a) 155 Å, (b) 125 Å, and (c) 40 Å. ....	64
4.2	PTEM micrographs of the 155 Å specimen at (a) 15 and (b) 45 min, the 125 Å specimen at (c) 15 and (d) 45 min, and the 40 Å at (e) 15 min and (f) 45 min upon annealing at 750 °C. ....	65
4.3	Defect densities for the 180, 155, 125, 80, and 40 Å specimens annealed at 750 °C.....	66
4.4	Trapped interstitial concentrations for the 180, 155, 125, 80, and 40 Å specimens annealed at 750 °C.....	67
4.5	Dislocation loop component of the overall defect density for the 180, 155, 125, 80, and 40 Å specimens annealed at 750 °C.....	68

4.6	{311} defect component of the overall defect density for the 180, 155, 125, 80, and 40 Å specimens annealed at 750 °C. ....	69
4.7	Dislocation loop component of the overall trapped interstitial concentration for the 180, 155, 125, 80, and 40 Å specimens annealed at 750 °C.....	70
4.8	{311} defect component of the overall trapped interstitial concentration for the 180, 155, 125, 80, and 40 Å specimens annealed at 750 °C. ....	71
4.9	Average dislocation loop diameter for the 180, 155, 125, 80, and 40 Å specimens annealed at 750 °C.....	72
4.10	Average {311} defect length for the 180, 155, 125, 80, and 40 Å specimens annealed at 750 °C.....	73
4.11	Trapped interstitial concentration with respect to amorphous layer depth for the 10 keV Ge <sup>+</sup> implant following a 750 °C anneal for 15 and 45 min.....	74
5.1	Comparison of amorphous layer depth measurements between ellipsometry and high resolution transmission electron microscopy following a 400 °C anneal over time. ....	78
5.2	Reduction in amorphous/crystalline interface roughness as measured by high-resolution transmission electron microscopy following a 400 °C anneal. ....	79
5.3	High-resolution transmission electron microscopy cross section images of 5 keV, 1 x 10 <sup>15</sup> Ge <sup>+</sup> cm <sup>-2</sup> implant annealed at 400 °C for (a) 0 min, (b) 40 min, and (c) 80 min.....	80
5.4	High-resolution transmission electron microscopy cross section images of 10 keV, 1 x 10 <sup>15</sup> Ge <sup>+</sup> cm <sup>-2</sup> implant annealed at 400 °C for (a) 0 min, (b) 40 min, and (c) 80 min.....	81
5.5	High-resolution transmission electron microscopy cross section images of 30 keV, 1 x 10 <sup>15</sup> Ge <sup>+</sup> cm <sup>-2</sup> implant annealed at 400 °C for (a) 0 min and (b) 40 min.....	82

Abstract of Thesis Presented to the Graduate School  
of the University of Florida in Partial Fulfillment of the  
Requirements for the Degree of Master of Science

DISSOLUTION AND SURFACE PROXIMITY EFFECTS OF LOW ENERGY,  
AMORPHIZING GERMANIUM IMPLANTS INTO SILICON

By

Andrew C. King

December 2003

Chair: Kevin S. Jones

Major Department: Materials Science and Engineering

As CMOS device dimensions are scaled laterally to increase the density of transistors per die, they also must be scaled vertically. Thus, it becomes increasingly important to understand the interactions of the silicon surface with point defects. Preamorphization is a common method for preventing channeling of implanted ions deep into the silicon crystal. Reducing the preamorphization implant energy effectively places the end-of-range (EOR) damage closer to the surface. How the EOR damage evolves has a critical effect on the amount of dopant diffusion that occurs. Speculation remains over how the excess interstitial population in the EOR is affected by the surface as the preamorphization energy is reduced.

The first experiment in this thesis characterizes the damage created by a 5 keV,  $1 \times 10^{15} \text{ Ge}^+ \text{ cm}^{-2}$  implant into silicon, which evolves much differently than higher energy implants. Using plan-view transmission electron microscopy, it was found that small, unstable dislocation loops formed in the EOR with a dissolution activation energy of 1.13

$\pm 0.14$  eV. The defects were shown not to coarsen significantly, but rather just decrease in number before the rapid dissolution took place. A surface lapping experiment showed that the defect dissolution energy is not attributed to the increased proximity of the surface, but was in fact implant energy related. The amorphous layer of a 10 keV,  $1 \times 10^{15}$  Ge<sup>+</sup> cm<sup>-2</sup> implant, which forms {311} defects and later stable dislocation loops, was reduced to less than that of the 5 keV implant and annealed at 750 °C. The defect evolutions were then quantified for the 5, 10, and 10 keV-lapped samples. It was found that the defect evolution for the 10 keV-lapped specimen strongly resembles that of the control, un-lapped 10 keV sample.

In the second experiment in this thesis, the effect of surface proximity for shallow amorphous layers was further studied. The amorphous layer of a 10 keV,  $1 \times 10^{15}$  Ge<sup>+</sup> cm<sup>-2</sup> implant was reduced from 180 Å to depths of 155, 125, 80, and 40 Å. The samples were then annealed at 750 °C for 15 and 45 min, and the defect populations were analyzed using plan-view transmission electron microscopy. Results show that increased surface proximity on amorphizing implants does not cause a significant reduction in the trapped interstitial concentration even down to amorphous layer depths of 40 Å.

The final experiment examines the effect of a low temperature anneal on the accuracy of ellipsometry measurement of shallow amorphous silicon layers on the surface of crystalline silicon substrates. It was shown that a 400 °C anneal significantly improves the accuracy of the ellipsometry measurements and does not regrow the amorphous layer. A reduction in the amorphous/crystalline interface roughness from the anneal was correlated to the increase in accuracy.

## CHAPTER 1 INTRODUCTION

### **1.1 Background and Motivation**

Modern day computing power is based on the integrated circuit (IC), which is a large number of transistors, resistors, capacitors, and other devices wired together on a the same substrate to perform a designated circuit function. The invention of the IC is attributed to Jack Kilby of Texas Instruments and Robert Noyce of Fairchild Semiconductor in 1959 [1]. Since then, the number of components on a typical IC has gone from the tens to the tens of millions.

In 1965 Gordon Moore [2], an executive at Intel, made the observation that in order for the semiconductor industry to meet market demands, the number of transistors on the IC would have to double every 1 to 2 years. This observation has since come to be known as “Moore’s Law,” and has served as the industry trend and key indicator in predicting cutting-edge semiconductor technology for the past 30 years.

In the late 1990’s experts in the semiconductor industry from Europe, Japan, Korea, Taiwan, and the USA developed the International Technology Roadmap for Semiconductors (ITRS) [3], which presents a semiconductor industry-wide consensus on the research and development needs for the industry over a 15 year time span. The primary focus of the ITRS is to maintain the continued scaling trends of ICs that require increasing the packing density, speed, and power efficiency of devices on the scale of

Moore's Law. These trends are ultimately responsible for decreasing the cost-per-function of ICs, which has led to significant improvements in productivity and quality of life through the proliferation of computers and other electronic devices.

The metal-oxide-semiconductor field-effect-transistor (MOSFET) is the basic building block of the IC (Figure 1). The scaling trends established by the ITRS require reducing the feature size of the MOSFET with every new generation of devices to meet performance requirements. One of the most challenging problems of device scaling is forming highly doped, ultra-shallow source/drain junctions and extensions with low sheet resistance. With each successive technology node, the junction depths are required to scale with the gate length to avoid short channel effects. These effects result when the drain's electric field penetrates through the channel region and affects the potential barrier between the source and the channel regions. These effects diminish the ability of the gate to control the channel charge.

ITRS also requires increasingly higher doping concentrations of the junctions to account for the inverse relationship between sheet resistance and junction depth. Shallower junctions will ultimately have higher resistivity. In physical terms, a deeper junction has a larger volume and therefore can incorporate a larger dose of electrically active carriers than a shallow junction with the same concentration, thus achieving a lower sheet resistance. Table 1 shows the 2002 ITRS junction-doping requirements projected to the 2016 technology node.

Currently ion implantation is the preferred method of forming shallow junctions due its precision in controlling dopant concentrations and profiles. Implanting arsenic into the crystalline silicon forms shallow  $n^+$ -p junctions with relative ease due to arsenic's

heavy atomic mass and small projected range. However, shallow  $p^+n$  junctions are difficult to form due to the p-type dopant's small atomic mass, boron. When boron is implanted into silicon, channeling of the boron ion occurs. This results in a dopant profile channeling tail and a much deeper junction [4].

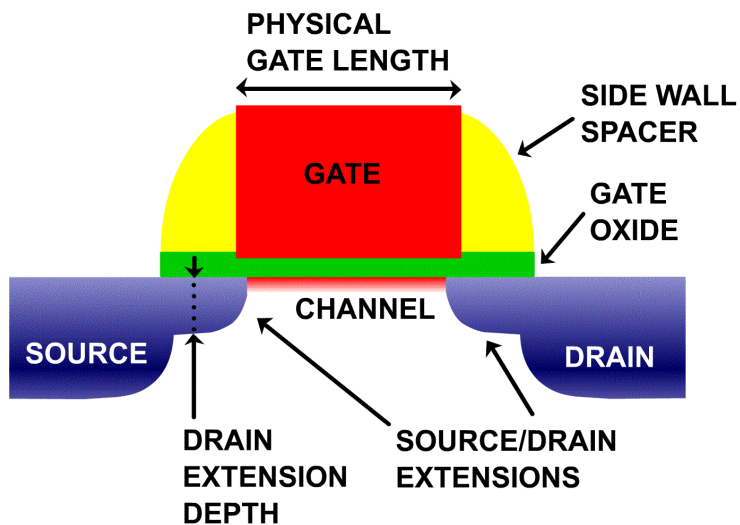


Figure 1.1 Cross-sectional schematic of a MOSFET.

Amorphizing the silicon substrate by implanting isoelectric species such as silicon [5] or germanium [6] prior to dopant implantation (preamorphization) has been shown to reduce the channeling tail of boron. In fact, the channeling tail can be completely eliminated if the entire boron profile is within the amorphous region [7]. Subsequent recrystallization of the amorphous layer by solid phase epitaxy (SPE) [8] has been found to result in high dopant activation as well as reduced diffusion of dopant [9,10].

The major drawback to the preamorphization technique is the formation of extended defects below the original amorphous/crystalline ( $\alpha/c$ ) interface following SPE. These defects are referred to as end-of-range (EOR) damage since they reside at the end of the projected range of the implanted species. EOR damage can have detrimental

affects on junction performance. If the EOR region is located within the depletion region of the device, large leakage currents will result [11]. Also, the supersaturation of interstitials in the EOR region can lead to transient enhanced diffusion (TED) [12] of the dopant profile, resulting in a deeper junction.

Table 1.1 2002 ITRS doping technology requirements [3].

<b>Year of Production</b>	<b>2001</b>	<b>2004</b>	<b>2007</b>	<b>2010</b>	<b>2013</b>	<b>2016</b>
Technology Node (nm)	130	90	65	45	32	22
MPU, Functions per chip (Gbits)	0.54	1.07	4.29	8.59	34.36	68.72
Physical Gate Length (nm)	65	37	25	18	13	9
Contact $X_j$ (nm)	48-95	27-45	18-37	13-26	10-19	7-13
Drain extension $X_j$ (nm)	27-45	15-25	10-17	7-12	5-9	4-6
Max Drain extension $R_s$ (PMOS) ( $\_ /sq.$ )	400	660	760	830	940	1210
Max Drain extension $R_s$ (NMOS) ( $\_ /sq.$ )	190	310	360	390	440	570
Extension lateral abruptness (nm/decade)	7.2	4.1	2.8	2.0	1.4	1.0

Despite the difficulties presented by EOR damage, preamorphization is a necessary process step in novel dopant activation techniques that are being developed to meet future ITRS technology nodes, such as solid phase epitaxy regrowth (SPER) [13], laser thermal processing (LTP) [14], and flash lamp annealing [15]. Therefore it is important to understand the parameters involved in EOR damage evolution in order to accurately model dopant diffusion in silicon, which is a key factor in the continued scaling of junctions.

## 1.2 Ion Implantation

Ion implantation is the primary technology for introducing impurities into semiconductors to form devices and IC circuits. The ion implantation process is highly flexible in the selection of dopant species, in choosing the spatial location to implant the

species, and in its superior concentration profile control. The process consists of accelerating a beam of ions with sufficient energy to penetrate the target material.

As the incident ions enter the substrate they undergo two stopping processes, nuclear and electronic stopping [16]. Nuclear Stopping ( $S_n$ ) occurs from collisions of the incident ion and the core electrons of the substrate atoms.  $S_n$  interactions usually involve an energy transfer during the collision between the ions and the atoms large enough to displace the substrate atoms from their lattice positions. This can lead to a damage collision cascade where many nuclear events can be produced by one primary ion. The large amount of damage produced by collision cascades from  $S_n$  can form continuous amorphous layers in silicon substrates. Electronic stopping ( $S_e$ ) arises from collisions between the incident ions and the outer electron shells of the substrate atoms.  $S_e$  interactions are similar to a drag force exerted on the implanted ions, transfer much less energy, and produce negligible damage to the substrate.

The depths that the ions reach, or travel before they come to rest, in the target substrate follows an approximate Gaussian form, where the peak of the distribution corresponds to the most probable projected ion range. This is referred to as the projected range ( $R_p$ ), and the standard deviation of the distribution is called the straggle ( $\Delta R_p$ ).  $R_p$  depends mainly on the energy and mass of the implanted species, while  $\Delta R_p$  depends on the ratio of the mass of the implanted ion to the mass of the substrate atom.

During the ion implantation process, combinations of interstitial and vacancy pairs are created. These are called Frenkel pairs. A Frenkel pair is created during an individual ion collision event when the implanted ion collides with a lattice atom and knocks it out of position. The removed atom becomes an interstitial while a vacancy is

created in the lattice position where the atom was removed. Additionally, if the interstitial produced by the initial collision has sufficient energy, it may knock off other atoms from lattice position creating additional Frenkel pairs in a multiplying nature.

Mazzone [17] used Monte Carlo calculations to show that the vacancies and interstitials in the Frenkel pairs reside at different regions of the ion-depth profile. The calculations predict that the forward peaking nature of the momentum of an incoming ion produces a vacancy-rich zone in the region extending from the surface down to about  $0.8R_p$  while between  $R_p$  and  $2R_p$ , there should be a interstitial-rich zone. Due to non-conservative nature of ion implantation, meaning that substitution atoms are introduced into the lattice in far excess of available unoccupied lattice sites, the interstitial component dominates the point defect distribution for low to medium implant energies ( $<$  a few hundred keV) [18].

During a post-implant anneal in non-amorphized silicon, excess interstitials in the lattice have been observed due the damage created during implantation [19-21]. During annealing, vacancies are recombined with interstitials, but the non-conservative nature of implantation creates excess interstitials. Giles [19] proposed the “+1” model, which suggests that one interstitial, is created for each implanted ion during annealing and their diffusion is limited to either the surface or further into the substrate.

During the ion implantation process, the irradiation of silicon can produce a crystalline-to-amorphous phase transition if a critical dose for amorphization is achieved. As mentioned previously, amorphizing silicon eliminates channeling of boron, and the SPE regrowth of the amorphous layer enhances electrical activation of the implanted dopant. The amorphization phase transition begins when sufficient irradiation from the

ion beam produces a defected crystalline lattice with the same free energies as an amorphous silicon network.

Holland et al. [22] proposed a model that considers the amorphization of silicon as critical-point phenomenon where the onset of amorphization leads to a cooperative behavior among various defects types that results in a greatly accelerated transition. Through their experiment with silicon self implants, a dose dependence of damage production was determined with two different regimes: an initial regime where growth is constrained by the formation simple point defects, followed by a regime of unconstrained growth which results in the complete amorphization of the lattice. In the latter regime, the onset of amorphization is precipitated by the rapid growth of damage that results from a cooperative mechanism where amorphous regions preferentially sink interstitial point defects which promotes more damage and leads to further amorphization.

Another mechanism of amorphization from ion implantation proceeds by gradual changes occurring to the lattice over a range of doses. The process starts by the formation of small, isolated pockets of amorphous material. As the dose increases the pockets increase in number and overlap until eventually all the pockets have overlapped and a continuous amorphous layer is present.

Typically amorphization of silicon is done with  $^{28}\text{Si}^+$  or  $^{73}\text{Ge}^+$  [6] since they are isoelectric and do not interfere with electrically active dopants. Clark [23] studied the effect of increasing the preamorphizing species' mass on the formations of ultra-shallow junctions. It was determined that ions with larger atomic mass units are more efficient in amorphizing silicon, which results in less interstitial injection in the EOR region following SPE and less TED.

### 1.3 Solid Phase Epitaxy

The recrystallization mechanism of implanted amorphized silicon is called solid phase epitaxy (SPE). SPE proceeds epitaxially on an underlying crystalline silicon substrate. It is layer-by-layer laminar growth with atomic step edges as growing sites. Typical SPE regrowth begins to occur at temperatures as low as ~400-450 °C [24, 25] and on up to temperatures just below the melting point of amorphous silicon with regrowth rates dramatically increasing for increasing temperature. This is due to the fact that SPE recrystallization rates follow an Arrhenius expression determined by Csepregi et al. [8, 26]

$$v = v_0 e^{-\left(\frac{E_a}{kT}\right)} \quad 1.1$$

where  $v$  is the regrowth velocity,  $v_0$  is the pre-exponential factor,  $E_a$  is the activation energy,  $k$  is Boltzmann's constant, and  $T$  is temperature in degrees Kelvin. Their work also showed that the orientation of the silicon also heavily determines recrystallization rates, reporting that  $\langle 100 \rangle$  silicon regrows at a rate about 3 times faster than  $\langle 110 \rangle$  silicon and about 25 times faster than  $\langle 111 \rangle$  silicon. Experiments on determining the activation energy and pre-exponential factor have produced varied results. Licoppe and Nissim [27] report values of  $3 \times 10^8$  cm/sec and 2.7 eV for  $v_0$  and  $E_a$  respectively, while Olson [28] found values of  $3.07 \times 10^8$  cm/sec and 2.68 eV for  $v_0$  and  $E_a$  respectively. In general, amorphous silicon regrows at a rate of  $10 \text{ \AA} / \text{s}$  at 600 °C [13].

After the amorphous layer has regrown, the resulting recrystallized material is largely defect free and better quality than irradiated silicon that was not amorphized. The SPE process also produces high electrical activation of dopants because during regrowth

impurities may become trapped onto substitution lattice sites allowing metastable conditions to be met. However, after regrowth the region just below the original amorphous/crystalline interface will have a supersaturation of interstitials and will probably form extended defects depending on the annealing conditions.

#### **1.4 End-of-Range Damage**

The regrowth of amorphized silicon leaves a supersaturation of interstitials in the region just beyond the original amorphous/crystalline interface, which consolidates into extended defects during annealing. There are two sources of the interstitials that lead to the formation the extended defects. The first source is transmitted ions, which are the ions that come to rest below the amorphous/crystalline interface. The second source is the recoiling of excess interstitials deeper into the material due to the forward momentum of the ion beam. Jones et al. [29, 30] classifies this form of ion implantation induced damage as Type II or end-of-range (EOR) damage. The concentration of interstitials in the EOR region is sufficient to form both dislocation loops and  $\{311\}$  defects, which are described below. One interesting aspect of EOR damage is that the concentration of defects is not strongly dependant on dose [29, 30], but does change with implant energy [6, 31].

Dislocation loops in the EOR region are either  $\{111\}$  faulted Frank dislocation loops, or  $\{111\}$  perfect prismatic dislocation loops [32]. These loops are metastable defects consisting of interstitial silicon atoms.  $\{311\}$  defects, or rod-like defects, consist of silicon interstitials condensed on the  $\{311\}$  habit plane and elongated in the  $[110]$  direction.

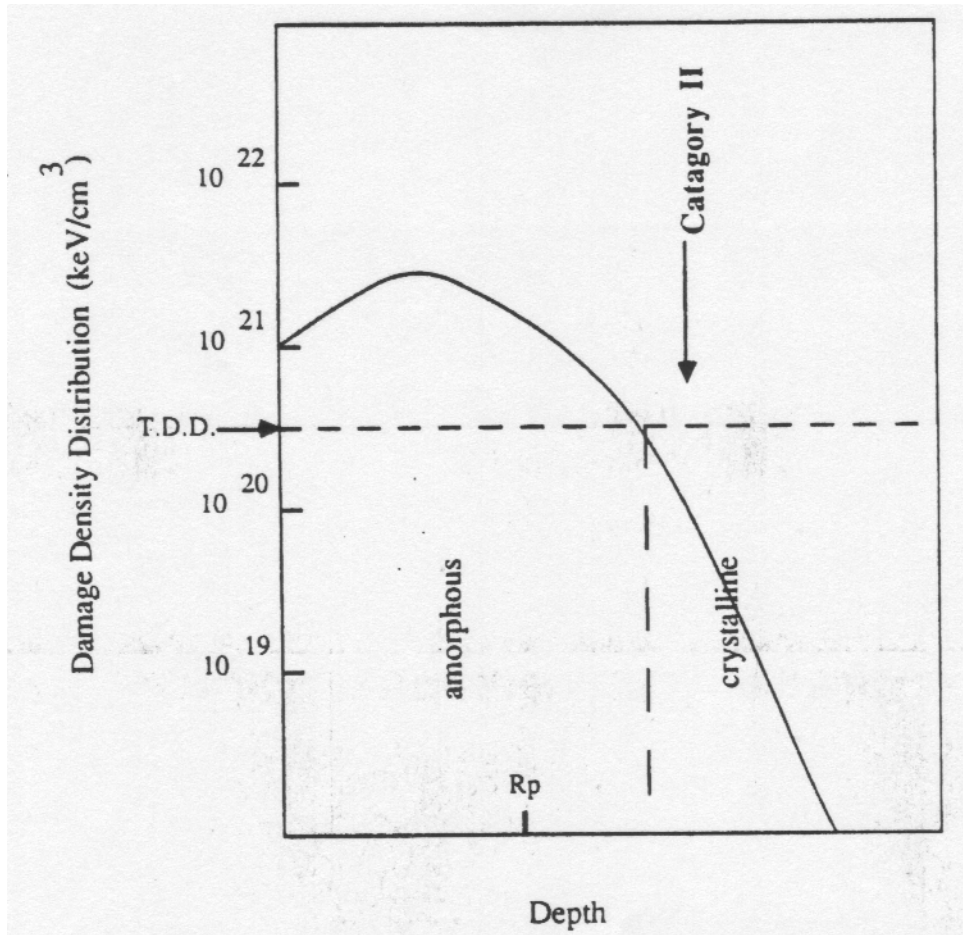


Figure 1.2 EOR damage created from an amorphizing implant [30].

#### 1.4.1 Defect Evolution

The excess interstitials in the EOR created by the ion implantation process are mobile at high temperatures, and undergo extensive diffusion during annealing where they can coalesce into either dislocation loops or  $\{311\}$ 's in order to conserve free energy. Robertson et. al [33] used transmission electron microscopy (TEM) to observe that EOR defects formed by a 20 keV  $1 \times 10^{15} / \text{cm}^2$   $\text{Si}^+$  implant undergo an evolution during annealing at 750 °C over an extended period of time (10-370 min). The study showed that after 10 minute, both  $\{311\}$  defects and small dislocation loops are present,

and as annealing times progressed the  $\{311\}$  defects followed two evolutionary pathways; faulting to form dislocation loops or dissolving releasing interstitials. Figure 1.3 shows a defect evolution tree from Jones [34].

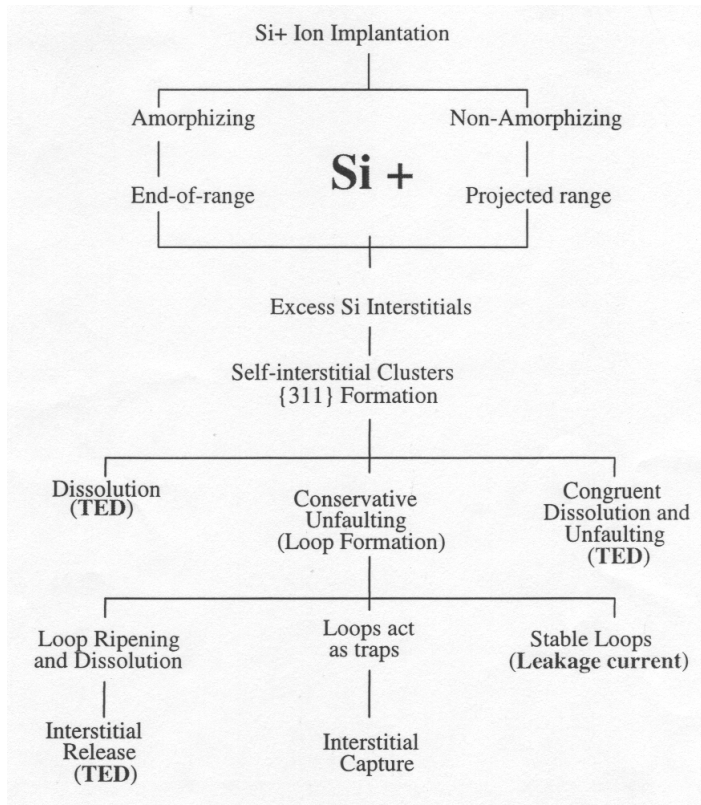


Figure 1.3 Defect evolution of excess interstitials resulting from ion implantation into silicon and subsequent annealing [34].

The  $\{311\}$  defect evolution shows that compared to dislocation loops,  $\{311\}$ 's are metastable and become unstable at lower interstitial supersaturation. Therefore when the supersaturation of interstitials fall below a critical point, dislocation loops become energetically favorable and  $\{311\}$ 's undergo unfauling to form dislocation loops [20, 35]. Also, the dissolution of  $\{311\}$  defects release interstitials that were trapped, which can lead to TED [36].

Dislocation loops have a formation threshold higher than  $\{311\}$  defects making loops less favorably during early annealing times. However, dislocation loops are more

thermodynamically stable than  $\{311\}$ 's, therefore they can exist at longer times and higher temperatures. Stolk et al. [37] reported an activation energy for  $\{311\}$  dissolution to  $3.8 \pm 0.2$  eV while previous studies of dislocation loop dissolution in silicon have always shown an activation energy of 4 - 5 eV [38]. During the anneal the defect evolution of dislocation loops undergoes four stages: nucleation, growth, coarsening, and dissolution [39]. For short times during the nucleation stage, a large portion of interstitials precipitate to form dislocation loops while a small percent diffuses down the gradient. In the pure growth stage the supersaturation of interstitials is too low to form new loops, so loops grow but the density of defects remains unchanged. For long annealing times Ostwald ripening occurs, where the dislocation loops are in dynamic equilibrium with the surrounding excess interstitials, resulting in the growth of large dislocation loops at the expense of smaller ones [40, 41].

Gutierrez [42] examined the EOR defect evolution of 5-30 keV  $1 \times 10^{15}$  Ge<sup>+</sup> cm<sup>-2</sup> at 750 °C using TEM and observed similar results as Robertson [33] for the 10 and 30 keV implant energies, interstitials evolving from small clusters to  $\{311\}$  defects and then to loops. However, for the lowest energy, 5 keV, the interstitials form small, unstable dislocation loops that dissolve within a narrow time window, with no  $\{311\}$  formation. This result suggests that for low energy amorphizing implants there may be a different defect evolution.

#### **1.4.2 Transient Enhanced Diffusion**

In addition to forming extended defects, the excess interstitials created by ion implantation causes an enhancement [40, 43] of the diffusion of the dopant profile which is a major challenge in the formation of ultra-shallow junctions. An excellent review of

TED is provided by Jain et al. [44] The origin of TED is based on the results of annealing a boron implanted silicon sample at  $\sim 800$  °C. During the anneal boron in the tail of the implanted profile diffuses very fast, faster than the normal thermal diffusion by a factor of 100 or more. After annealing for a while, the enhanced diffusion saturates. The enhanced diffusion is temporary, on annealing the same sample again after the saturation, enhanced diffusion does not occur again, hence transient enhanced diffusion.

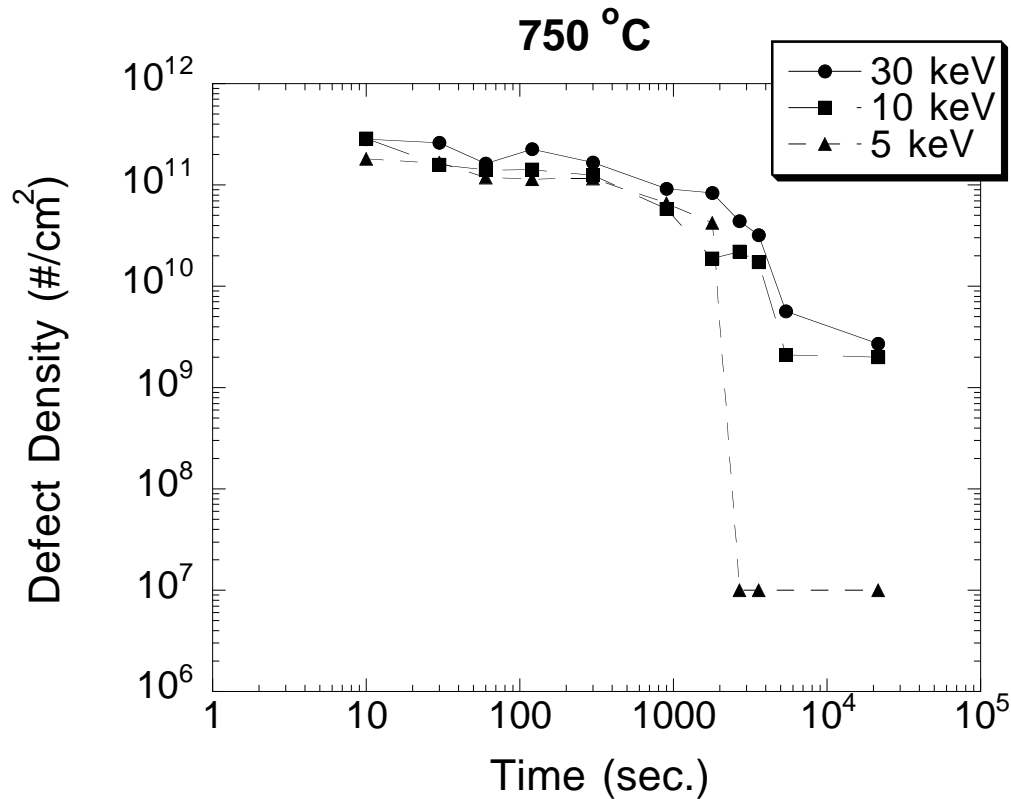


Figure 1.4 Defect evolution reported by Gutierrez [42] for  $\text{Ge}^+$  implanted at energies of 5, 10, and 30 keV at a constant dose of  $10^{15} \text{ cm}^{-2}$  annealed at 750 °C.

For the case of amorphizing implants, the enhanced diffusion is limited to the interactions between interstitials in the EOR region and the boron atoms [12, 20]. Both {311} defects and dislocation loops can drive TED in amorphizing implants. Eaglesham

et al. [20] and Jones [45] found the dissolution of {311}'s in the EOR region correspond to the same time interval as TED, which is consistent with assertion that {311} defects are the source of the interstitials. Also, Lampi et al. [39] proposed that the evolution process of dislocation loops not only affects the time interval of TED, but also implies that loops are a source of interstitials as well. Robertson et al. [46] suggested that the dissolution rate of {311} defects alone is not sufficient to drive TED and loop growth, but is assisted by the dissolution of sub-microscopic interstitial clusters.

Therefore, the dissolution of interstitials from different defect morphologies affect TED, but the degree of to which defect contributes is dependent on dissolution rate and activation energy of a given interstitial precipitate. The dissolution rate of the defect will determine the rate at which interstitials are released, while the activation energy of a defect will determine the whether or not the interstitial precipitate will dissolve at a given temperature.

### **1.5 Effect of the Free Surface on End-of-Range Damage**

As mentioned above, the excess interstitials introduced from ion implantation are believed to have two annealing sites, either the wafer surface or the bulk. It has widely been proposed that the wafer surface is an infinite interstitial recombination sink; therefore, as device scaling trends require shallower amorphous layers, the excess interstitials in EOR damage will be in ever increasing proximity to the surface. Surface effects on the formation and evolution of extended defects in the EOR and on TED are a controversial topic and have produced studies with contradicting results.

Meekinson [47] using controlled etching reduced the thickness of a 3900 Å amorphous layer to 2000 Å and 800 Å and then annealed the samples in nitrogen ambient

at 1100 °C. TEM showed that the number of interstitials in EOR dislocation loops decreased with a decrease in amorphous layer thickness. The study also reported dislocation loops in the shallower amorphous layers lost interstitials from dislocation loops at a faster rate than in the sample with the original amorphous layer thickness. A similar study by Narayan et al. [48] reported a similar effect. They attributed this effect to either the reduced distance between interstitials and the surface or glide of the loops to surface due to an image force.

Raman et al. [49] created EOR dislocation loops 2600 Å deep after annealing an amorphizing dual implant of 120 keV and 30 keV  $10^{15}$  Si<sup>+</sup>/cm<sup>2</sup> at 850 °C for 30 min. A CMP procedure was used to remove various amounts silicon in order to reduce loop depth in samples to 1800 and 1000 Å. They found that the proximity to the surface significantly affected dissolution kinetics of dislocation loops, and that loops dissolution is diffusion limited to the surface. However, in this experiment the effect of amorphous layer thickness was not a variable since the CMP procedure was performed after the amorphous layer was recrystallized.

A model proposed by Omri et al. [50] considers the amorphous/crystalline interface as a diffusion barrier for interstitials during the nucleation state of extended defects, when the supersaturation is high. Then, according to their model, only after SPE regrowth during the coalescence of loops when the supersaturation of interstitials is high the surface can act as a recombination sink. In their experiment a 150 keV  $2 \times 10^{15}$  Ge<sup>+</sup> cm<sup>-2</sup> implant was used to create a 175 nm thick amorphous layer. Anodic etching was used to vary the thickness of the amorphous layer from 175- 30 nm that were annealed at 1000 and 1100 °C for 10s. Using TEM they observed that despite the varied amorphous layer

thickness, the population of loops were the same. It was concluded that only after the amorphous layer has fully regrown interstitials can recombine at the surface. However, when this occurs the defects are already involved in the coarsening process and the supersaturation is small which tends to diminish the effect of the surface.

Ganin and Marwick [51] observed similar results to Omri. They compared the EOR damage created by a 40 keV and 200 keV amorphizing  $\text{In}^+$  implants and then reduced the depth of the amorphous layer of the 200 keV implant to the sample thickness of the 40 keV sample. This enabled them to study the effect of surface proximity on EOR damage upon annealing. It was concluded that the damage created from the implants was strongly energy dependent since the 200 keV sample with reduced amorphous layer had the same EOR damage as a normal 200 keV implant.

### **1.6 Scope and Approach of this Study**

The work in this thesis is divided into three experimental sets. In the first experiment, the defect dissolution observed by Gutierrez for the 5 keV,  $1 \times 10^{15} \text{ Ge}^+ \text{ cm}^{-2}$  implant condition will be further investigated. This investigation will entail determining the defect dissolution activation using a time – temperature study, qualifying the role of increased surface proximity on the dissolution, and simulating implant conditions using UT-Marlowe.

The second experiment in this thesis is a surface lapping experiment which will help to enhance the understanding of increased surface proximity on interstitials in the EOR region for low energy implants. In this experiments the amorphous layer of a 10 keV,  $1 \times 10^{15} \text{ Ge}^+ \text{ cm}^{-2}$  implant will be lapped to various thicknesses and annealed. Influence of surface proximity will then be quantified using plan-view TEM.

The final section of this thesis is a quick experiment that will measure the effect of a low temperature pre-anneal on the accuracy of shallow amorphous layer thickness measurements using ellipsometry. The results of all three of these experimental sections as well their contributions to understanding of extended defect formation in ion implanted silicon will be discussed. Finally, avenues of future experiments will be discussed.

## CHAPTER 2 EXPERIMENTAL AND DATA EXTRACTION PROCEDURES

In this chapter, an overview of the sample preparation, characterization techniques, and data extraction procedures for the three experiments will be given.

### 2.1 Transmission Electron Microscopy

Transmission electron microscopy (TEM) is a very useful technique for imaging extended defects created from the ion implantation process. Both diffraction and imaging information can be obtained with TEM based on the interactions between the electron beam and a thinned specimen as the beam transmits through that specimen. Specimens can be viewed from both the top down orientation or in cross section to give a three-dimensional perspective on the damage created.

Viewing specimens from the top down orientation is referred to as plan-view transmission electron microscopy or PTEM. PTEM allows the imaging of extended defects (dislocation loops and  $\{311\}$  defects and quantification of defect evolution. Defects are visible in PTEM according to diffraction contrast if  $\mathbf{g} \cdot \mathbf{b} \times \mathbf{u} \neq 0$  where  $\mathbf{g}$  is the reciprocal lattice vector corresponding to the diffraction plane,  $\mathbf{b}$  is the dislocations Burgers vector, and  $\mathbf{u}$  is the dislocation line direction. All PTEM specimens were viewed on JEOL 200CX operating at 200 keV in the  $\mathbf{g} \cdot 3\mathbf{g}$  centered weak beam dark field (WBDF) condition using a  $\mathbf{g}_{220}$  two-beam imaging condition at a magnification of 50,000 X. The WBDF field condition is very useful in imaging defects since it only resolves the

region of the highest strain around an extended defect, which is the core of the dislocation [52].

Viewing specimens in cross section is appropriately referred to as cross section transmission electron microscopy (XTEM). A JOEL 2010 high-resolution TEM operating at 200 keV as well as a JOEL 200CX operating at 200 keV were used to measure amorphous layer thickness down the [110] zone axis.

### **2.1.1 Plan-view Transmission Electron Microscopy Sample Preparation**

Plan-view transmission electron microscopy (PTM) samples are prepared in order to view the TEM specimen from the top-down orientation. The samples are made according to the following procedure:

1. A 3 mm disc is cut out of experimental material with a Gatan ultrasonic disc cutter using silicon carbide (SiC) powder abrasive and water. The sample is mounted on a glass slide with the top - side (implanted side) down with crystal bond. Crystal bond is a thermoplastic that softens with the application of heat and hardens at room temperature. For all application involving crystal bond a hot plate is used as the heat source (set to ~ 200 °C) and acetone is used to remove the crystal bond from the specimen. The glass slide is then adhered to the disc cutters stage using double-sided tape.
2. The sample is then thinned to approximately 100  $\mu\text{m}$  using abrasive slurry of 15  $\mu\text{m}$  aluminum oxide ( $\text{Al}_2\text{O}_3$ ) powder and water on a glass plate. The sample is mounted top-down on a metal stage using crystal bond. The stage is attached to a handheld lapping fixture from South Bay Technology and

lapped in figure eight motions until the sample is deemed thin enough by finger touch.

3. The sample is then further thinned using a wet drip etch of 25% hydrofluoric acid (HF) and 75% nitric acid (HNO<sub>3</sub>). The sample is etched by mounting it top - side down on a Teflon stage with paraffin wax. The wax is melted on a hot plate and is used coat the top - side to prevent etching of the implanted surface. The sample is then adhered to the stage by coating the perimeter of the sample with wax leaving the center of the sample uncovered to allow preferential etching of the sample center. Etching is deemed complete when a hole is created and a red transmission under a light source can be observed around the edges of the etch pit.
4. The sample is then removed from the Teflon mount and soaked in n-heptane for 15 min – 24 hr or until all wax has been removed. The sample is now ready for PTEM.

### **2.1.2 Cross-Section Transmission Electron Microscopy Sample Preparation**

Cross-section transmission electron microscopy (XTEM) samples are prepared using either two techniques of the following techniques. The first technique is performed according to the following procedure:

1. Two 20 milli-inch wide strips are cut with a high - speed wafer dicing saw from the experimental material.
2. The two strips are glued together using a thermally activated two-component epoxy with the surfaces of interest facing each other. Then two dummy strips of the same width are glued to both sides of the experimental

strips making 6 strips total glued together. The epoxy is then cured on a hot plate at  $\sim 200$  °C for 10 minutes to ensure proper cross-linking.

3. A 3 mm disc is cut from the glued strips using the same procedure outlined in the above section.
4. The disc is then mechanically thinned on both sides using a progressive sequence of gritted carbide lapping papers. The lapping is performed in an up and down motion using a handheld lapping fixture.
5. The sample is further thinned using a VCR Dimpler. In this procedure the disc is mounted on a thin sapphire disc with crystal bond and mounted on the Dimpler stage. The sample is first flattened using the appropriate flattening polishing wheel and 3  $\mu\text{m}$  slurry to 100  $\mu\text{m}$ . The center of the sample, or the interface of the two center strips, is then dimpled using the dimpling polishing wheel and 1  $\mu\text{m}$  slurry until a red transmission under light can be observed on the interface. Then a fine polishing wheel is used with a 0.1 and 0.05  $\mu\text{m}$  slurry to remove scratches on the dimpled surface created during the thinning process.
6. The sample is then ion milled using  $\text{Ar}^+$  in a dual-gun Gatan ion mill set at 12-14° tilt until a small hole created on the interface of the center strips is created. The sample is now thin enough for XTEM.

The second technique uses a Strata Dual Beam 235 FIB (focused ion beam) from FEI, Inc to cut out a XTEM specimen that is approximately 18  $\mu\text{m}$  long, 3  $\mu\text{m}$  deep, and 1500 Å thick using a gallium ion source. The sample is first coated with carbon followed by a layer of platinum that is approximately 1  $\mu\text{m}$  thick. Once the specimen is cut out, it

is mounted on a copper specimen ring with carbon mesh. The FIB XTEM is now ready for TEM.

### **2.1.3 Extraction of Defect Parameters from PTEM**

Determining defect parameters from PTEM images, such as defect density, trapped interstitial concentration, and defect sizes, allows for the quantification of how interstitials evolve over time at a specific annealing temperature. Understanding the influence of implant energy, implanted species, annealing temperature, annealing time and other factors on the damage created helps provide experimental results to assist dopant diffusion models, such as FLOOPS [53], to correlate TED and the evolution of EOR damage. There is an intrinsic 20 % error associated with the following methods for extracting defect parameters [54].

#### **2.1.3.1 Extraction of Defect Densities from PTEM**

Defect density is simply the number of defects observed in PTEM in the area that they were observed in. The defect densities in this study are determined by the following procedure adapted for one set forth by Bharatan [54]:

1. PTEM negatives are enlarged to 3X (making total magnification now 150 kX) and printed onto 8" x 10" photographic paper.
2. A transparent film with a grid of 4 cm x 4 cm squares printed on it is laid on top of the print. All resolvable defects (defect clusters, dislocation loops, {311}'s) within a given square are carefully traced onto the transparency with a fine tip marker.
3. The defect density is then determined by dividing the total number of defects counted by the area of the square,  $16 \text{ cm}^2$ , and multiplying by the magnification to the second power. This is done from at least three of the

squares on the transparency in random areas and the results are averaged together.

This process is adapted to counting only specific defects as well. To determine the {311} defect density, only {311} defects are traced and counted in the given area, and to determine the dislocation loop density only dislocation loops are counted. The detection limit of defects for PTEM is considered to be  $10^7$  defects /  $\text{cm}^2$

### **2.1.3.2 Extraction of Trapped Interstitial Concentrations from PTEM**

The trapped interstitial concentration gives a quantity of the number of silicon interstitial atoms present in the defects observed. The PTEM detection limit of trapped interstitials is considered to be  $6 \times 10^9$  interstitials /  $\text{cm}^2$ . The first steps are the same as in the procedure for determining defect density. Dislocation loops and {311} defects are traced separately on transparencies. Then the following steps are taken:

1. The traced transparencies are scanned into *.pict*-formatted files using Adobe Photoshop software.
2. The scanned file is imported into an image analysis program developed by the National Institute of Health called NIH Image v.1.6.1. The software measures the length sum of {311} and the total area of dislocation loops.
3. The {311} defect trapped interstitial concentrations are determined by calculating a modified length sum by the linear density of interstitials (26 interstitials / nm) contained in the {311} defect and dividing by the scanned area. The modified length sum is used for {311} type defects imaged at a  $45^\circ$  angle to the imaging plane because the length observed is a projected length of the defect and not the actual length. In order to account for the discrepancy, these defects' lengths are multiplied by a factor of 1.4.

4. Dislocation loop trapped interstitial concentrations are calculated by dividing the total area of the loops by the area of the scanned image and multiplying the result by the planar atomic density of the  $\{111\}$  plane which is  $1.6 \times 10^{15}$  atoms / cm<sup>2</sup>.

At this point it is important to note that in his thesis, Gutierrez [42] assumed the small defects created by the 5 keV energy to be dislocation loops and extracted trapped interstitial concentrations using the above method. In this present work this assumption is made also. Support for the assumption that the small defects observed in the TEM from the 5 keV implant are dislocation loop – like will be shown in Chapter 3.

## **2.2 Variable Angle Spectroscopic Ellipsometry**

Ellipsometry is an optical technique that measures the change in polarized light as it is reflected off a sample. Variable angle spectroscopic ellipsometry (VASE) is used in this work as a fast, nondestructive technique for measuring amorphous silicon layer thickness, in contrast to XTEM. In VASE a linearly polarized light is reflected off the surface of the sample into a detector. As the polarized light reflects off the surface the light changes from plane-polarized light into elliptically polarized light. The elliptically polarized light is characterized as having two electric field components perpendicular to one another and a phase difference,  $\Delta$ . It is  $\psi_r$ , which is the azimuth of the reflected light, and  $\Delta$  that are characteristic of the material under study and are measured for sample analysis. Once the optical constants ( $\psi_r$  and  $\Delta$ ) are measured, a computer program constructs a model to solve for layer thickness based on a library of previously measured constants.

All VASE measurements were performed using a J. A. Woolmam multi-wavelength spectroscopic ellipsometer with a 75 W xenon light source at a fixed angle of 75°. The system is first calibrated by measuring the silicon dioxide thickness on a calibration wafer. The only sample preparation required in VASE is a careful cleaning of the sample's surface with methanol. The sample area must be larger than 1 cm x 1 cm to eliminate edge effects from the light source's beam, which is about 3 mm in diameter. During measurements a fixed 20 Å oxide layer was assumed for samples to account for the native oxide of silicon. A minimum of three measurements is taken from different areas on the sample for all measurements.

The VASE technique produces very precise measurements, but the accuracy may some time be questionable. Scanning over a larger range of wavelengths of light also increases accuracy of measurements. Overall the VASE system normally yields an accuracy of 10-20% of actual thickness determined from TEM, however Lindfors[10] showed that very shallow amorphous layer the accuracy may be worse. In his work he measured an amorphous layer thickness of a 2.5 keV  $1 \times 10^{15} \text{ Si}^+ / \text{cm}^2$  to be 26 Å with high-resolution TEM compared to 13 Å with VASE.

### **2.3 UT – Marlowe**

UT – Marlowe [55] is a binary collision approximation simulator that considers crystal structure, therefore it is used for the simulation of ion implantation into crystalline and amorphous material. This modeling predicts both the impurity profiles as a function of depth of implant parameters and also damage profiles, which can be used as input files for TED simulators, such as FLOOPS (see section below).

During this work UT- Marlowe has been used to simulate the 5 and 10 keV  $1 \times 10^{15}$  Ge<sup>+</sup>/cm<sup>2</sup> amorphizing implants in order to give a qualitative understanding of the initial implant conditions and the difference of the net excess interstitials (NEI) in the EOR region created between the two energies. UT-Marlowe can simulate amorphous layer depths by using the *filename.rbs* output file, which simulates a rutherford backscattering spectrometry (RBS). The amorphous layer depth is determined by finding the depth at which the percentage of amorphization decreases most rapidly on a linear - linear plot.

The NEI is calculated by using two separate output files. The first output file used is the *filename.ist* output file. It is the concentration of silicon interstitials formed during implantation at a given depth. When the concentration of interstitials reaches  $5 \times 10^{21}$  cm<sup>-3</sup> or 10% of the lattice density at a given depth the lattice is considered amorphized. The second output file used is the *filename.vac* file. It provides a concentration of concentration profile of the number of silicon vacancies formed during implantation. Subtracting the concentration profile of interstitials from the concentration profile of the vacancies in the EOR region and taking the integral of the area underneath the difference calculate the NEI. The NEI is the difference between two very large numbers therefore the simulation was performed with 300,000 input ions.

#### **2.4 5 keV Ge<sup>+</sup> Defect Dissolution Study**

The goal of this study is to gain further understanding of the defect dissolution observed by Gutierrez [42] for the 5 keV  $1 \times 10^{15}$  Ge<sup>+</sup> cm<sup>-2</sup> implanted silicon wafers. The first experiment in this study was performed to calculate the activation energy of the observed defect dissolution. The second experiment was performed to determine if the

increased surface proximity for the 5 keV energy (amorphous layer thickness =  $100 \text{ \AA}$ )<sup>1</sup> compared to the 10 keV energy (amorphous layer thickness =  $220 \text{ \AA}$ )<sup>2</sup> has a role in the dissolution process. For both experiments the source material used is Czochralski grown (100) Si wafers implanted by Varian, Inc. at room temperature with a constant dose of  $1 \times 10^{15} \text{ Ge}^+ \text{ cm}^{-2}$  at 5 and 10 keV energies with a  $7^\circ$  tilt. These wafers have only a native oxide layer, approximately  $20 \text{ \AA}$  thick. Finally, UT – Marlowe was used to obtain a qualitative understanding of the difference in the NEI difference between the two energies in the EOR region.

#### **2.4.1 5 keV Defect Dissolution Activation Energy Experiment**

To investigate the defect dissolution process observed for the 5 keV energy implants, specimens were annealed at multiple temperatures to calculate the activation energy of the dissolution. PTEM was used to identify times when the dissolution process occurs at temperatures of 725, 750, 775, 825, and 875 °C. The times and corresponding temperatures were plotted in an Arrhenius-type chart to calculate the activation energy. The annealing was performed in a Lindberg tube furnace under nitrogen ambient with the sample placed in a quartz boat. All annealing procedures were performed in this furnace. Usually, samples are annealed first before they are thinned for TEM analysis, however Li[56] et al. showed once samples are thinned they can be annealed as well without producing a measurable effect on defect evolution. Based on this, many PTEM samples

---

<sup>1</sup> Values obtained from Gutierrez's work. The amorphous layer thickness for both energies are measured again in this work.

<sup>2</sup> Values obtained from Gutierrez's work. The amorphous layer thickness for both energies are measured again in this work.

in this work are annealed after they have been thinned to reduce the labor of sample preparation for every annealing time.

#### **2.4.2 Surface Lapping Experiment**

In the second part of this experiment the effect of increased surface proximity between the 5 and 10 keV implants was studied by using a mechanical lapping technique to bring the EOR region in the 10 keV implant to the same proximity to the surface as the 5 keV implant. In this experiment the amorphous layer of a 2 cm x 2 cm 10 keV Ge<sup>+</sup> sample was reduced to 80 Å, which is less than that of the amorphous layer of the 5 keV implant. The lapped sample was then annealed at 750 °C and the defect evolution was characterized using PTEM and compared to control samples of the 5 keV and 10 keV implants.

The mechanical lapping procedure used in the surface lapping experiment removes measured amounts of amorphous silicon in order to increase the surface proximity between the EOR region (and excess interstitials) to surface. The procedure used is based on the one developed by Herner et al [57]. The lapping procedure in this experiment was performed according to the following steps:

1. A 2 cm x 2 cm sample is cut from experimental material using a high - speed wafer dicing saw.
2. The square sample is then mounted on a lapping stage using crystal bond and lapped using a hand - lapping fixture from South Bay Technology and polished on 12 in rayon polishing pads with Syton® as the polishing agent. Syton® is colloidal silica with particle sizes from 0.2 – 0.6 µm. The sample is lapped in a figure eight motion. The lapping procedure removes about

10-12 Å per lap once the native oxide has been removed by the lapping procedure or by a buffered oxide etch (BOE).

3. Once the appropriate number of laps has been performed the sample is removed from the stage and the crystal bond is removed with acetone.

## 2.6 Surface Proximity Experiment

This experiment is a continuation of the surface lapping experiment described in the section above. The goal of this experiment is to determine what effect increased surface proximity has on excess interstitials in the EOR region. Three 10 keV,  $1 \times 10^{15}$  Ge<sup>+</sup> cm<sup>-2</sup> specimens with reduced amorphous layer depths of 155, 125, and 40 Å will be produced for this experiment in addition to the 80 Å specimen from the section above.

The procedures of this experiment is described below:

1. 2 cm x 2 cm samples are cut from experimental material using a high - speed wafer dicing saw and their amorphous layers are lapped using the procedure described in the above section.
2. Ellipsometry is then used to gain a quick measure of the lapped amorphous layer depths.
3. A 3 mm core is taken from the center of each of the 2 cm x 2 cm square samples and these cores are annealed at 750 °C for 15 min. The cored, annealed specimens are then thinned for PTEM. XTEM specimens are made from each of the square samples using a FIB to cut out a thin sample very close to area on the sample where the core was taken. The amorphous layer depths are then measured using XTEM.

4. PTEM is used to quantify the extended defects in the samples after the 15 min anneal, and then the samples are annealed for another 30 min making the total anneal time 45 min and examined with PTEM again.

The effect of increased surface proximity on interstitials in the EOR will be determined by comparing the defect parameters obtained by PTEM versus amorphous layer depths.

## 2.7 Ellipsometry Experiment

In this experiment, the effect of a low temperature anneal on the accuracy of ellipsometry measurements for shallow amorphous layers will be determined. The experimental material used in this experiment is 5, 10, and 30 keV,  $1 \times 10^{15} \text{ Ge}^+ \text{ cm}^{-2}$  implanted Si wafers from Varian, Inc. Samples from the wafers will be annealed at 400 °C for times ranging from 5 – 80 min in a conventional tube furnace with nitrogen ambient. Amorphous layer depths will then be measured using ellipsometry for each annealing time.

Ellipsometry measurements will be performed on a J. A. Woolmam multi-wavelength spectroscopic ellipsometer described in section 2.2. Three measurements will be performed on each sample. XTEM samples will be prepared for as-implanted specimens for the three implant energies as well as samples that have been annealed for 40 and 80 min. The XTEM specimens will be images on a JEOL 2010 high resolution TEM to image the amorphous layer depth as well as the amorphous/crystalline interface roughness. The amorphous/crystalline roughness will be determined by averaging peak-to-valley distance from five different positions along the interface from enlarged XTEM images.

## CHAPTER 3 5 keV Ge<sup>+</sup> DEFECT DISSOLUTION STUDY

### 3.1 Overview

The work in this chapter was performed to gain a better understanding of the defect dissolution observed by Gutierrez [42] for the 5 keV Ge<sup>+</sup> implant energy when compared to higher energies shown previously in Figure 1.4. In his thesis, Gutierrez reported the low energy implant created small unstable dislocation loops that dissolved rapidly after 60 min annealing time at 750 °C. Gutierrez concluded that the excess interstitials resulting from the 5 keV implant condition have an alternate evolutionary pathway than higher energy implants. The work in this chapter was performed to further characterize the previously unreported small unstable dislocation loops created from the low energy, amorphizing implant condition.

The first experiment in this chapter was performed to find the defect dissolution activation energy of the small defects created from the 5 keV implant. Since these small defects dissolve after shorter annealing times than ones created by the higher 10 and 30 keV implants, they must have a different dissolution energy threshold. The second experiment in this chapter was performed to determine the effect of increased surface proximity to the EOR region between the 5 and 10 keV implants. The 5 keV implant, reported by Gutierrez, forms a 100 Å amorphous layer compared to the 220 Å amorphous layer formed by the 10 keV energy. Therefore the diffusion distance to the surface for the interstitials created in the 5 keV implant is roughly half as far as it is for the

interstitials in the 10 keV case. If the surface acts like an infinite interstitial recombination sink then increased interstitial annihilation at the surface will lower the supersaturation and may account for the dissolution observed in the 5 keV implant. Finally in this chapter, initial implant conditions and the difference between the net excess interstitials (NEI) in the EOR will be calculated using UT-Marlowe simulations for the 5 and 10 keV energies.

### 3.2 Defect Dissolution Activation Energy

The defect dissolution activation energy for the 5 keV  $1 \times 10^{15} \text{ Ge}^+ \text{ cm}^{-2}$  implant condition was calculated by obtaining the times when all defects dissolved at 725, 750, 775, 825, and 875 °C using PTEM.

#### 3.2.1 TEM Results

Figures 3.1 – 3.5 show WBDF PTEM micrographs of the extended defects created by the 5 keV  $1 \times 10^{15} \text{ Ge}^+ \text{ cm}^{-2}$  implant at each of their respective times and temperatures until dissolution. As the micrographs show, the exact time when the defects dissolve is not determined since they are not annealed *in-situ* in the TEM, instead the dissolution time is determined by finding the range in time when the last point defects are present and next time where they are no longer present as observed by TEM. For example, at 725 °C the final annealing time defects were observed was at 70 min. At the next annealing time of 80 min, there are no observable defects and therefore they assumed to be dissolved. The time of defect dissolution at 725 °C is then to occur at a time between 70 and 80 min. Table 3.1 show the range of dissolution times determined by PTEM at each respective temperature.

Table 3.1 Time range where defect dissolution occurs at each annealing temperature as observed by PTEM.

Temperature	725 °C	750 °C	775 °C	825 °C	875 °C
Range	70 – 80 min	60 – 65 min	40 - 45 min	30 – 35 min	10 – 15 min

Figure 3.6 shows a WBDF PTEM image of a 5 keV implant annealed at 775 °C for 35 min imaged at the  $g_{040}$  condition in contrast to the normal  $g_{220}$  condition. The defect is faint, but shows two lobes with a line of no contrast through the middle that is parallel to  $g$ . This is characteristic to dislocation loop contrast in TEM [58]. This observation supports the assumption that the small defects created by the 5 keV energy implant are dislocation loops – like in nature.

Figures 3.7 and 3.8 show the defect density and trapped interstitial concentration trends over time at the five annealing temperatures, respectively. As the figures show, the defect densities and trapped interstitial concentrations decrease for increasing temperatures, as expected. Another trend that is clearly shown by the three lowest temperatures of 725, 750, and 775 °C is that the number of defects remains plateaued relatively high, in the  $10^{10}$  defect/cm<sup>2</sup> range until they approach their dissolution window where the trend decreases rapidly. The trapped interstitial concentration also shows this trend.

Figure 3.9 shows the average defect diameter over annealing at each of the five respective temperatures. The error bars represent the standard deviation of the averages. As annealing temperature increases, the average defect size increases. For the lowest annealing temperature, 725 °C, the defects do not increase in diameter or ripen over time significantly. At 15 min the average defect size is 5.89 nm and at the last point before

dissolution the average defect size has only increased to 8.92 nm. In general, the defects for all annealing times do not increase in average diameter greater than 40% before dissolution. The defects reduce in number more significantly than grow in size or coarsen.

### 3.2.2 Extraction of Defect Dissolution Activation Energy

The activation energy for the 5 keV,  $1 \times 10^{15} \text{ Ge}^+ \text{ cm}^{-2}$  implant defect dissolution was determined by applying an Arrhenius relationship to the time ranges and temperatures where the dissolution was observed, shown in Figure 3.10. The mid-point of the time ranges were plotted as a rate ( $\text{s}^{-1}$ ) on the y-axis with error bars reflecting the max and min of the time range. The inverse of temperature ( $\text{K}^{-1}$ ) was plotted on the x-axis multiplied by a factor of  $10^4$  for clarity.

Using a least square exponential curve fit to the data, the defect dissolution was found to follow the trend;

$$\tau = 99.845 e^{(-1.3091x)} \quad 3.1$$

The correlation coefficient,  $r$ , of the curve was determined to be 0.97091, which shows a strong fit to the data. The activation energy is determined by multiplying the fitted exponential value, 1.3091, by Boltzmann's Constant ( $8.65 \times 10^{-5} \text{ eV/K}$ ) and  $10^4$  to correct for the x-axis factor of the same value. Performing these operations reveals the ultimate trend of the defect dissolution, shown by the relationship;

$$\tau = \tau_0 e^{-(E_a/kT)} \quad 3.2$$

where  $E_a$  is 1.13 eV and  $\tau_0$  is  $99.845 \text{ s}^{-1}$ . The error that is associated with the experimentally determined  $E_a$  was determined to be  $\pm 0.14 \text{ eV}$ . This was calculated by fitting a line to plot in accordance with the maximum error represented by the error bars.

### 3.3 Surface Lapping Experiment

This experiment was performed to evaluate the effect of increased surface proximity on the dissolution of the defects created by the 5 keV,  $1 \times 10^{15} \text{ Ge}^+ \text{ cm}^{-2}$  implant. If the surface is a source for interstitial recombination, then the increased surface proximity in the 5 keV case may explain the rapid defect dissolution. In this experiment the amorphous layer of a 10 keV,  $1 \times 10^{15} \text{ Ge}^+ \text{ cm}^{-2}$  was lapped to thickness less than the thickness of 5 keV,  $1 \times 10^{15} \text{ Ge}^+ \text{ cm}^{-2}$  implant. Both the 5 and 10 keV energy implants were annealed at 750 °C for times ranging from 5 – 360 min and the defect evolution was characterized using PTEM.

#### 3.3.1 Amorphous Layer Lapping Results

Ellipsometry was used to determine if the 10 keV-lapped specimen's amorphous layer was polished to a thickness less than that of the 5 keV implant. Table 3.2 shows the ellipsometry measurement results for the 5, 10, and 10 keV-lapped specimens. Based on the ellipsometry results, the amorphous layer thickness for each specimen was verified using high - resolution transmission electron microscopy (HTREM). Figure 3.11 shows the HRTEM results. The amorphous layer thickness for the 5, 10, and 10 keV - lapped specimens was determined to be 100, 180, and 80 Å, respectively. The lapping procedure reduced the 10 keV-lapped specimen's amorphous layer thickness by 100 Å, 20 Å less than the 5 keV amorphous layer thickness.

Table 3.2 Ellipsometry measurements of amorphous layer thickness for the 5, 10, and 10 keV lapped specimens.

Amorphous layer thickness	5 keV	10 keV-lapped	10 keV
1 <sup>st</sup> measurement	144.24 Å	120.86 Å	209.54 Å
2 <sup>nd</sup> measurement	144.64 Å	118.20 Å	220.39 Å
3 <sup>rd</sup> measurement	144.04 Å	110.72 Å	226.25 Å

### 3.3.2 Defect Evolution

Figures 3.12 and 3.13 show PTEM micrographs of the defect evolution for the 10 keV specimen and the 10 keV-lapped specimen annealed at 750 °C. For micrographs of the 5 keV energy at 750 °C the reader is referred to Figure 3.2. It was found that the defect evolution of the 10 keV-lapped specimen strongly resembled that of the control, unlapped 10 keV specimen. Figure 3.14 shows the defect evolutions for the 5, 10, and 10 keV-lapped specimens. The 10 keV lapped specimen did not exhibit dissolution of defects, stable dislocation loops were still present after the longest annealing time of 360 min. The defect evolution for the 10 keV control and 10 keV-lapped followed that of the one reported by Gutierrez, small cluster defects evolved into {311} defects and dislocation loops, then [311] defects dissolved leaving stable dislocation loops.

### 3.4 UT-Marlowe Simulations

UT-Marlowe simulations were performed to obtain pre-experimental conditions of for the 5 and 10 keV,  $1 \times 10^{15} \text{ Ge}^+ \text{ cm}^{-2}$  implants. A 300,000-ion simulation was run for the two energies at a 7° tilt to match the implant conditions. The predicted amorphous

layer depths, vacancy profiles, interstitial profiles, and the net excess interstitial (NEI) profiles for the two energies were obtained.

### 3.4.1 Simulation Results

UT-Marlowe simulations for the 5 keV energy implant calculated a  $R_p$  of 70 Å and a  $\Delta R_p$  of 32 Å. Figure 3.15 shows the *.rbs* output for the 5 keV implant. The profile predicts the amorphous layer depth to be 108.3 Å compared to that of 100 Å measured by HRTEM. Figure 3.16 shows the vacancy and interstitial profile of the 5 keV implant. Note that the noise level in the data increases dramatically at concentrations below  $1 \times 10^{19} \text{ cm}^{-3}$ . UT-Marlowe simulations for the 10 keV energy implant calculated a  $R_p$  of 114 Å and a  $\Delta R_p$  of 53 Å. Figure 3.17 shows the *.rbs* output for the 10 keV implant. This profile predicts the amorphous layer depth to be 195.48 Å in contrast to 180 Å measured by HRTEM. Figure 3.18 shows the vacancy and interstitial profile of the 10 keV implant. Again, note that the noise level in the data increases dramatically at concentrations below  $1 \times 10^{19} \text{ cm}^{-3}$ .

### 3.4.2 NEI calculation

The NEI profiles for the 5 and 10 keV implants were obtained by normalizing the depth by eliminating the amorphous layer from the calculation and subtracting the interstitials from the vacancies in the profiles. The area under the curves up to a concentration of  $1 \times 10^{19} \text{ cm}^{-3}$  was then integrated to get the NEI concentration. Figure 3.19 shows the NEI profile for the two energies. The NEI concentration in the EOR region for the 5 keV implant was calculated to be  $3.47 \times 10^{14} \text{ cm}^{-2}$ . The NEI concentration in the EOR region for the 10 keV implant was calculated to be  $3.30 \times 10^{14} \text{ cm}^{-2}$ .

### 3.5 Discussion

The  $1.13 \pm 0.14$  eV defect dissolution activation energy for the 5 keV implant is an intriguing result, especially if these defects are considered to have a defect morphology like dislocation loops. These defects clearly do not behave like any type of dislocation loops previously reported in silicon, which have always had dissolution activation energies reported to be in the 4 – 5 eV range [59]. The explanation for this has always been that the Si self-diffusion was involved, which has an activation energy of  $\sim 4.5$  eV [59, 60]. The low 1.13 eV activation energy may indicate that instead of the dislocations moving by a diffusion controlled climb process, they dissolve by a lower energy glide process. Also, Figure 3.9 shows that the defects do not coarsen significantly, which is a key characteristic of dislocation loops.

One may propose that these defects are in fact spherical, or volumetric clusters of silicon interstitials, since that defect morphology would minimize the most energy. Calculating the trapped interstitial concentration assuming a sphere instead of plate will increase the value by a factor roughly of  $10^3$  interstitials/  $\text{cm}^2$ , which is an unreasonable value given the experimental conditions and results. Also, the appearance of the defect shown in Figure 3.6 is convincing evidence to the author that these defects are in fact plate-like, dislocation loops.

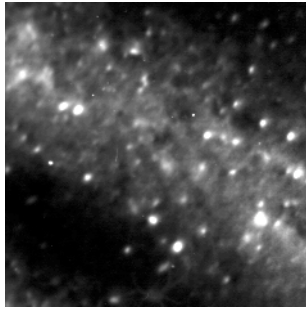
The surface lapping experiment eliminated surface proximity as the main factor responsible for the defect dissolution. The defects formed in the EOR are clearly implant energy dependent in agreement with Omri [50] and Ganin and Marwick [51]. UT-Marlowe simulations showed that there is no qualitative difference in the NEI in the EOR between the 5 and 10 keV energy implants, but the accuracy of these results are questionable. A simulation with a significantly larger amount of ions should be run to

further verify these results. Gutierrez [42] showed in his thesis using quantitative PTEM that there is almost an order of magnitude less trapped interstitials in the 5 keV case than in the 10 keV energy. Figure 3.20 shows his experimental results. The small, unstable defects may be a result from the implant condition that has a very small straggle, 32 Å, and a low supersaturation of excess interstitials.

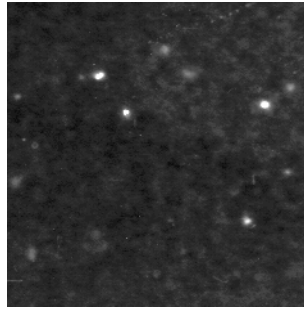
### 3.6 Conclusion

The small, unstable defects created by the 5 keV,  $1 \times 10^{15} \text{ Ge}^+ \text{ cm}^{-2}$  implantation into silicon reported by Gutierrez [42] were found to have a dissolution activation energy of  $1.13 \pm 0.14 \text{ eV}$ . PTEM showed that these defects do not significantly coarsen, but rather just decrease in number. A lapping experiment which reduced the amorphous layer of a 10 keV implant with the same dose to less than that of the 5 keV implant showed that increased surface proximity is not responsible for the defect dissolution. It was found that the defects in the 5 keV energy case were strongly implant energy dependent. The author proposes that these small defects are dislocation loop-like and are result of the implant's small straggle and low interstitial supersaturation.

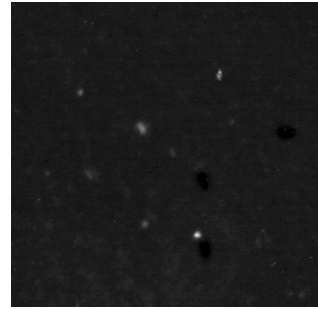
1000 Å



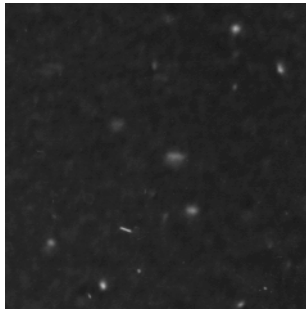
(a)



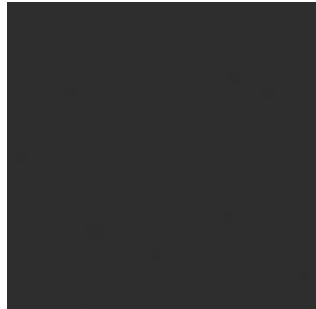
(b)



(c)



(d)



(e)

Figure 3.2 PTEM micrographs of 5 keV  $\text{Ge}^+$ ,  $1 \times 10^{15} \text{ cm}^{-2} \text{ Ge}^+$  annealed at 725 °C for (a) 15 min, (b) 60 min, (c) 65 min, (d) 70 min, and (e) 80 min.

1000 Å

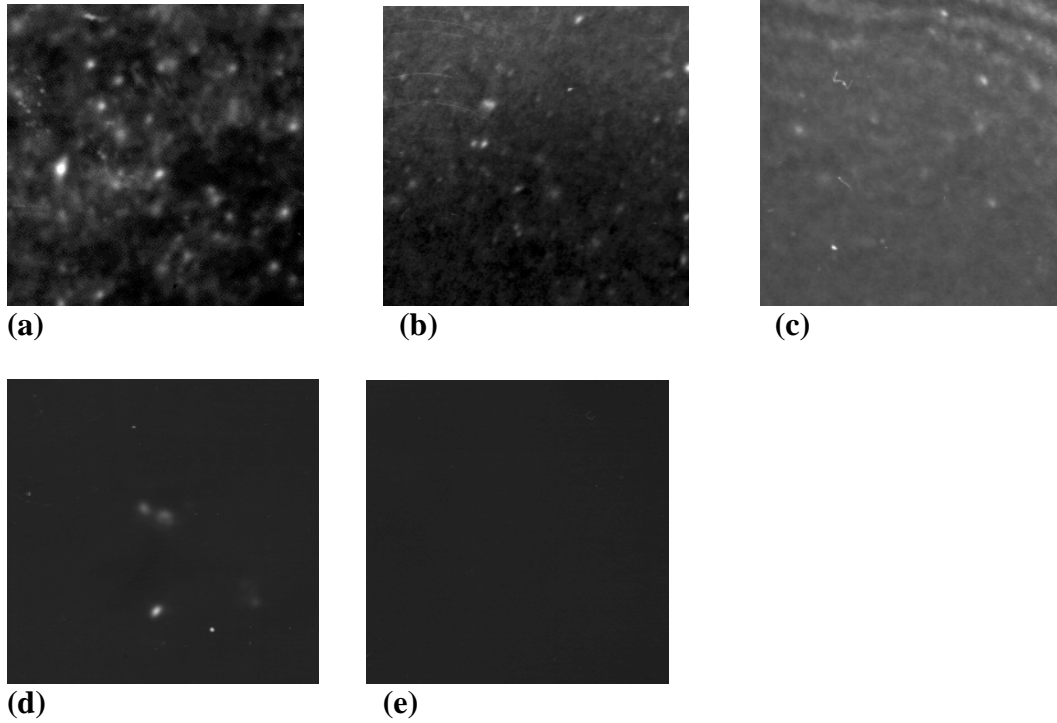
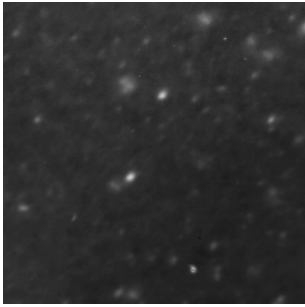


Figure 3.2 PTEM micrographs of 5 keV  $\text{Ge}^+$ ,  $1 \times 10^{15} \text{ cm}^{-2} \text{ Ge}^+$  annealed at 750 °C for (a) 5 min, (b) 15 min, (c) 45 min, (d) 60 min, and (e) 65 min.

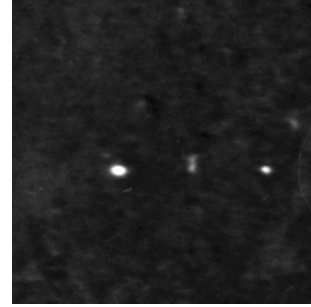
1000 Å



(a)



(b)



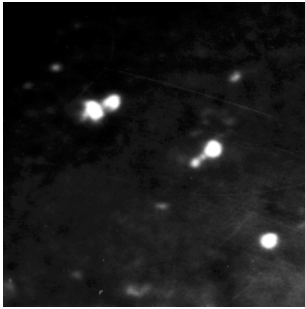
(c)



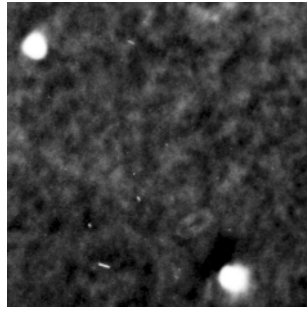
(d)

Figure 3.3 PTEM micrographs of 5 keV  $\text{Ge}^+$ ,  $1 \times 10^{15} \text{ cm}^{-2} \text{ Ge}^+$  annealed at 775 °C for (a) 15 min, (b) 35 min, (c) 40 min, and (d) 45 min.

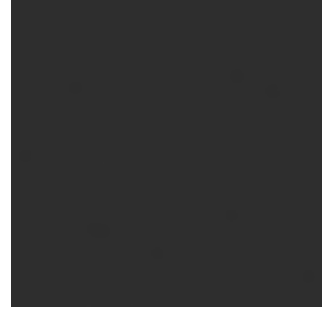
1000 Å



**(a)**



**(b)**



**(c)**

Figure 3.4 PTEM micrographs of 5 keV Ge<sup>+</sup>, 1 x 10<sup>15</sup> cm<sup>-2</sup> Ge<sup>+</sup> annealed at 825 °C for (a) 15 min, (b) 30 min, and (c) 35 min.

1000 Å

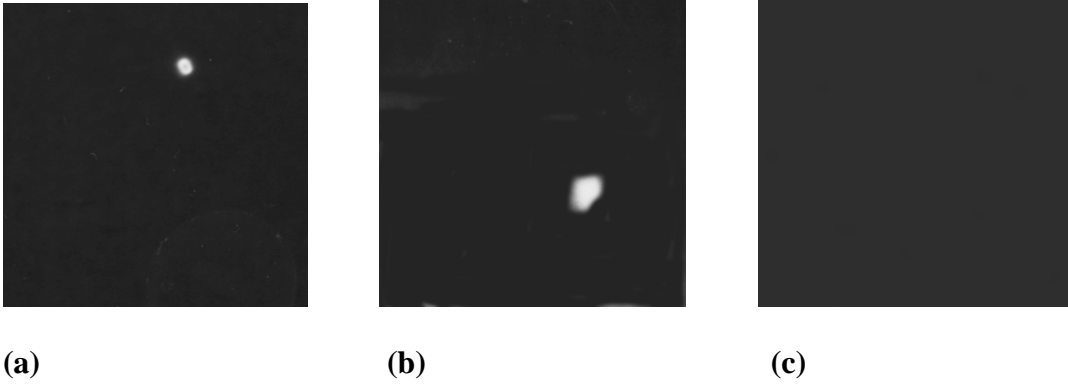


Figure 3.5 PTEM micrographs of 5 keV  $\text{Ge}^+$ ,  $1 \times 10^{15} \text{ cm}^{-2} \text{ Ge}^+$  annealed at 875 °C for (a) 5 min, (b) 10 min, and (c) 15 min.

300 Å

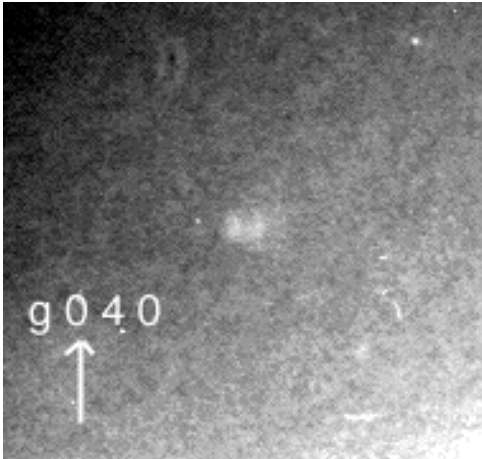


Figure 3.6 PTEM micrograph of 5 keV  $\text{Ge}^+$ ,  $1 \times 10^{15} \text{ cm}^{-2} \text{ Ge}^+$  annealed at 775 °C for 35 min imaged at the  $\mathbf{g}_{040}$  condition.

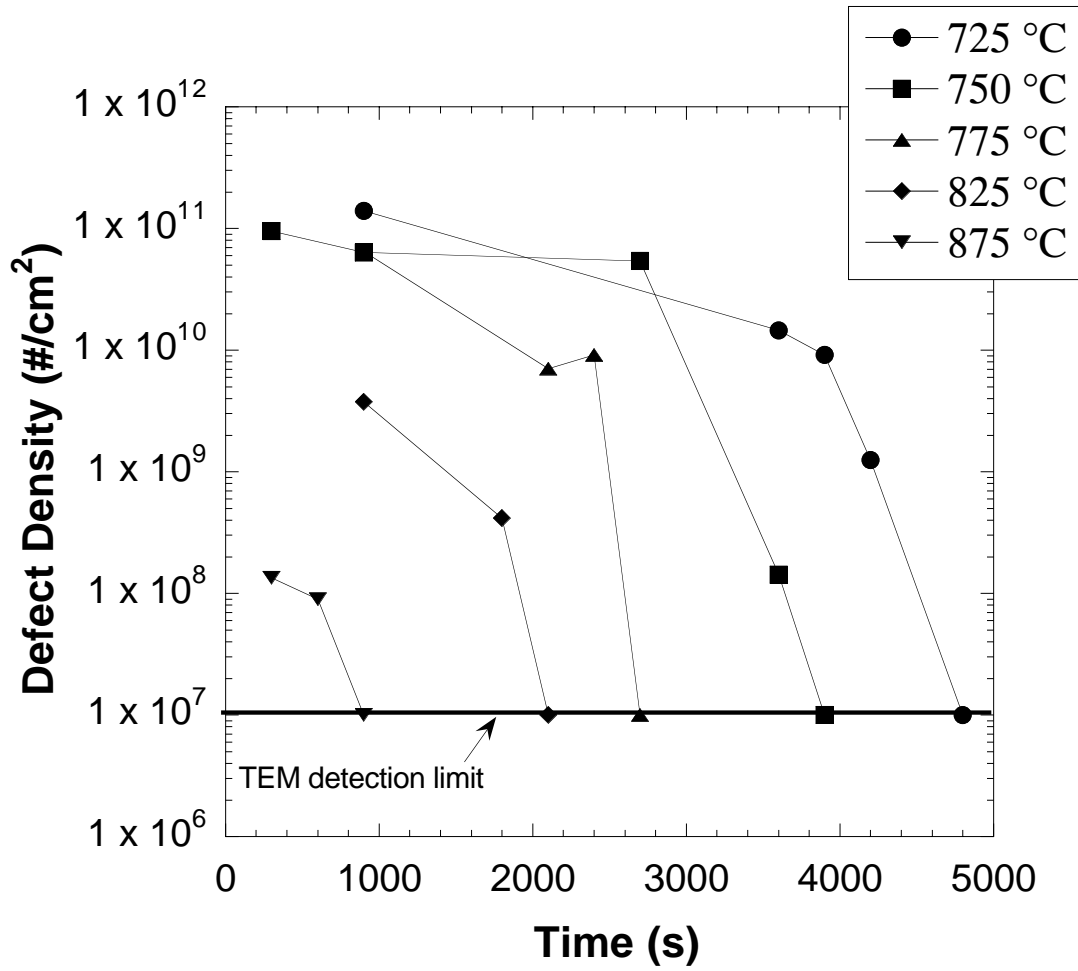


Figure 3.7 Defect density trends for 5 keV,  $1 \times 10^{15}$  Ge<sup>+</sup> cm<sup>-2</sup> implant over time annealed at 725, 750, 775, 825, and 875 °C.

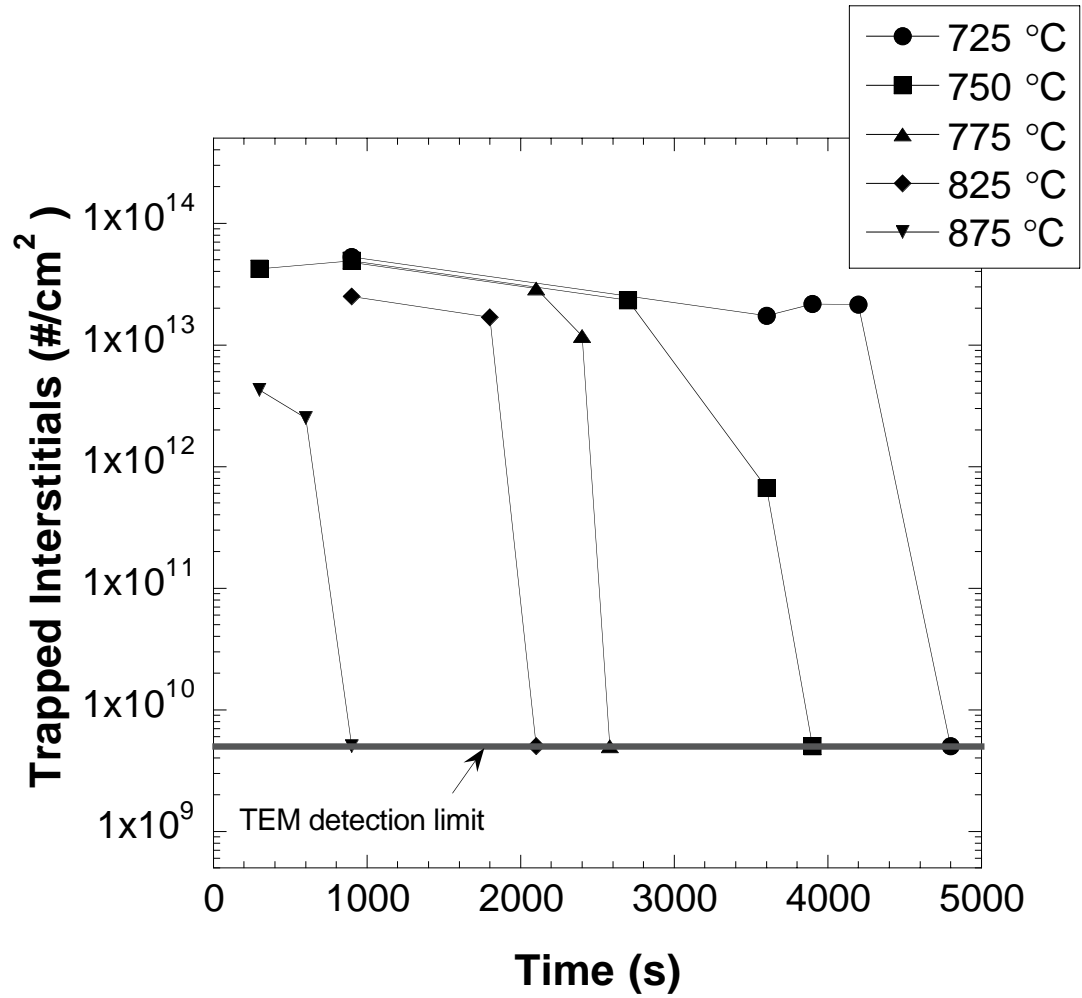


Figure 3.8 Trapped interstitial trends for 5 keV,  $1 \times 10^{15}$  Ge<sup>+</sup> cm<sup>-2</sup> implant over time annealed at 725, 750, 775, 825, and 875 °C.

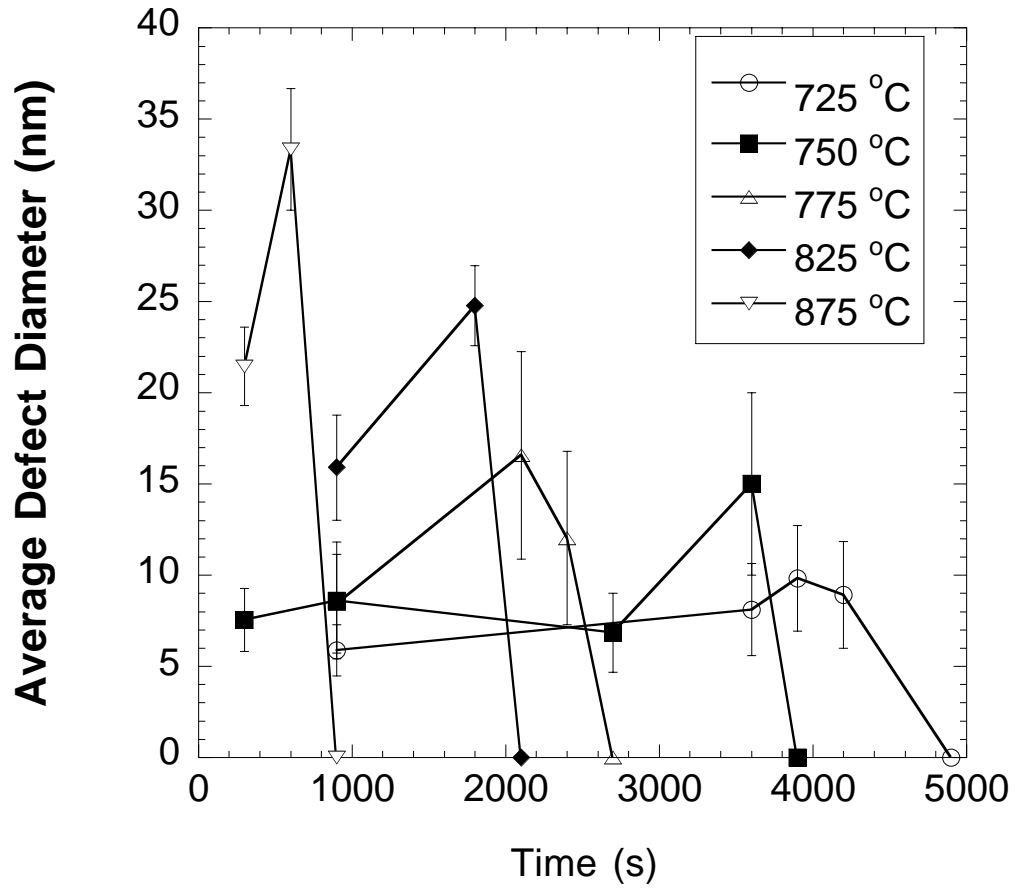


Figure 3.9 Average defect diameter over time for the 5 keV,  $1 \times 10^{15} \text{ Ge}^+ \text{ cm}^{-2}$  implant annealed at 725, 750, 775, 825, and 875 °C.

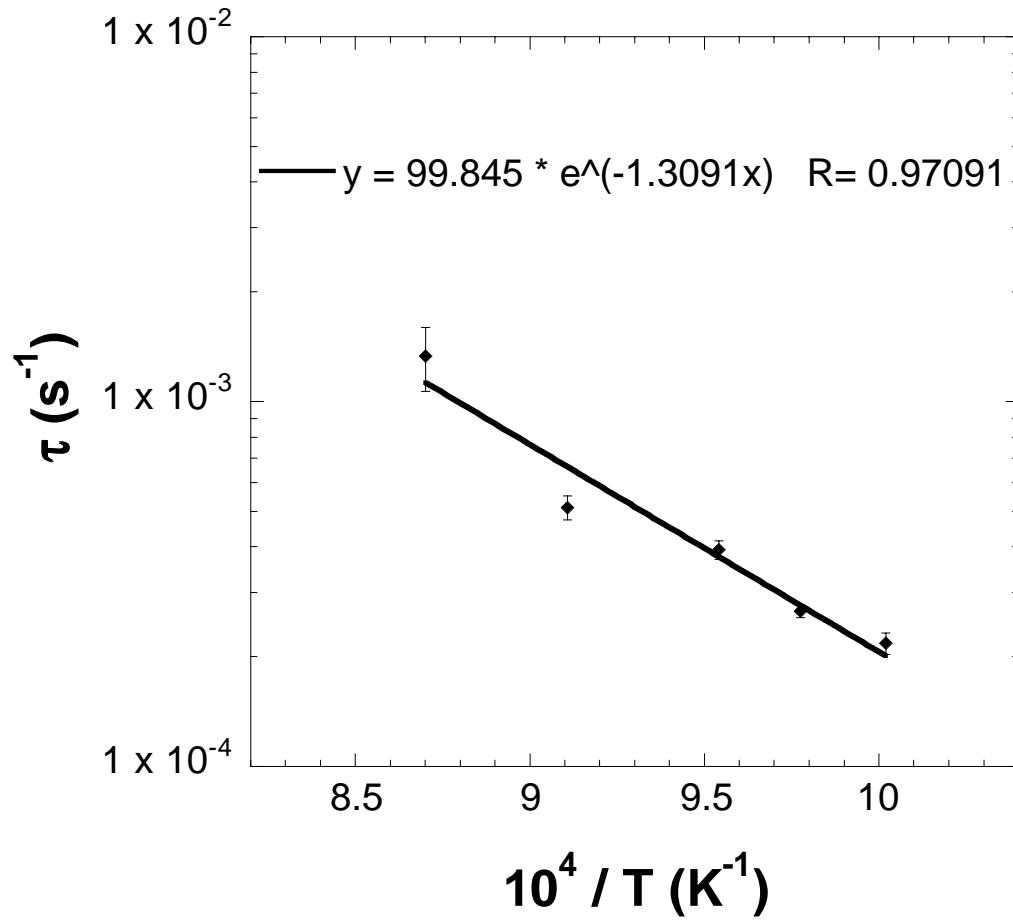


Figure 3.10 Defect dissolution rates versus inverse temperature, plotted in Arrhenius form. The trend is show as a least square exponential curve fit.

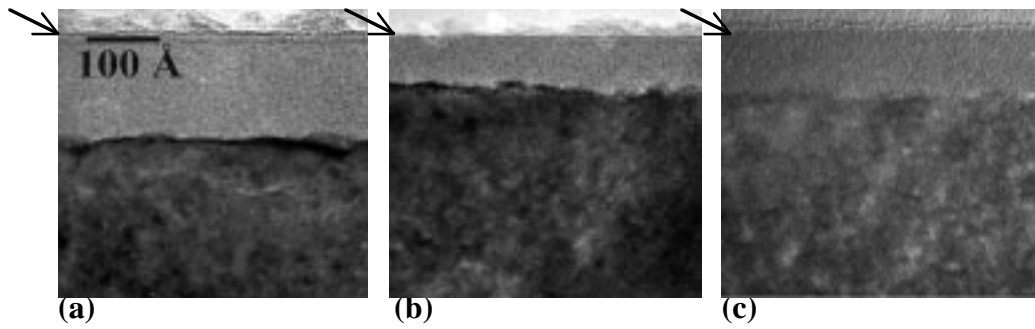


Figure 3.11 High-resolution cross section TEM micrographs of the amorphous layer thickness for (a) 10 keV, (b) 10 keV-lapped, and (c) 5 keV samples. Arrows point to the surface.

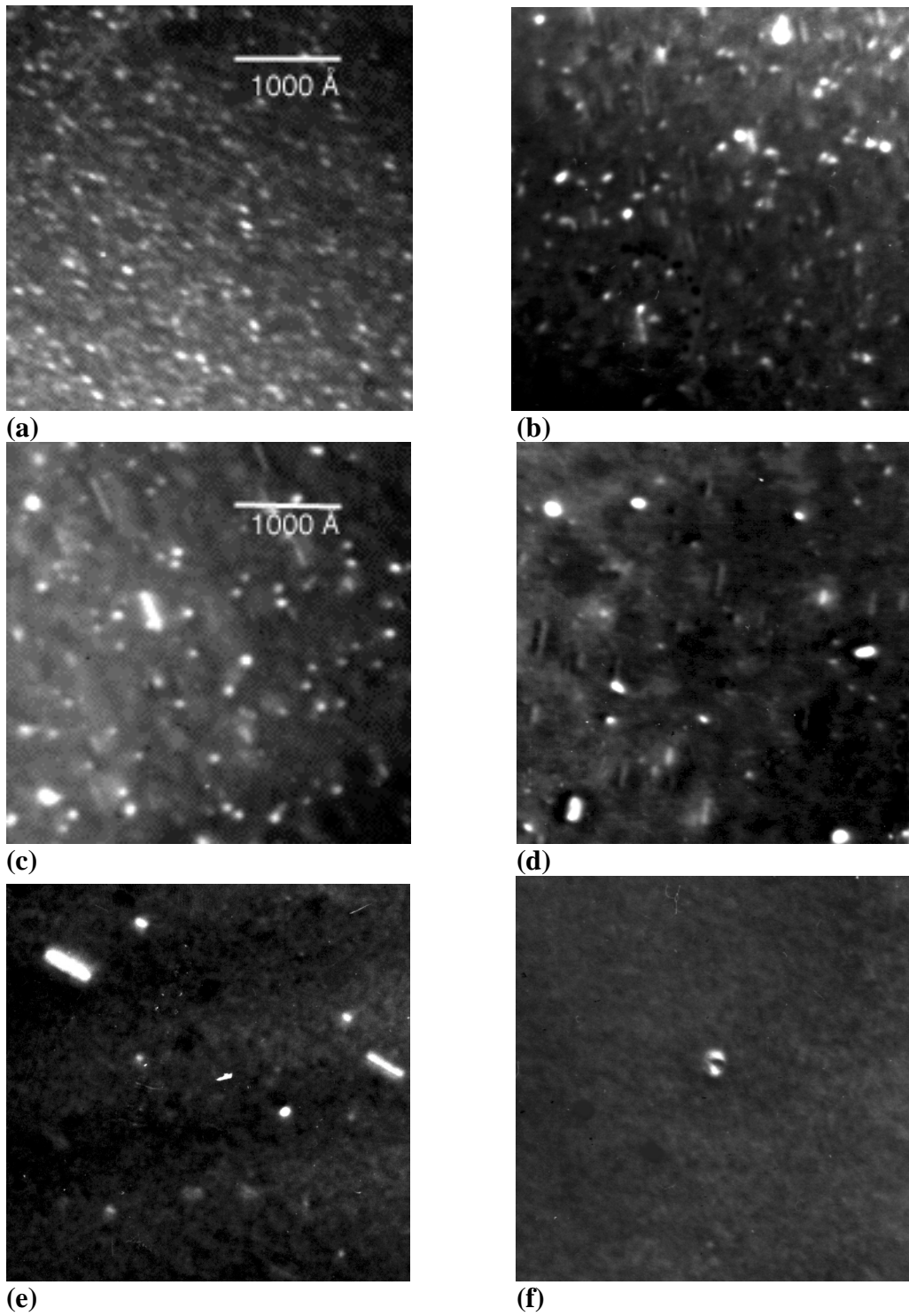


Figure 3.12 PTEM micrographs of the 10 keV Ge<sup>+</sup>,  $1 \times 10^{15} \text{ cm}^{-2}$  Ge<sup>+</sup> control implant annealed at 750 °C for (a) 5 min, (b) 15 min, (c) 30 min, (d) 45 min, (e) 60 min, and (f) 360 min.

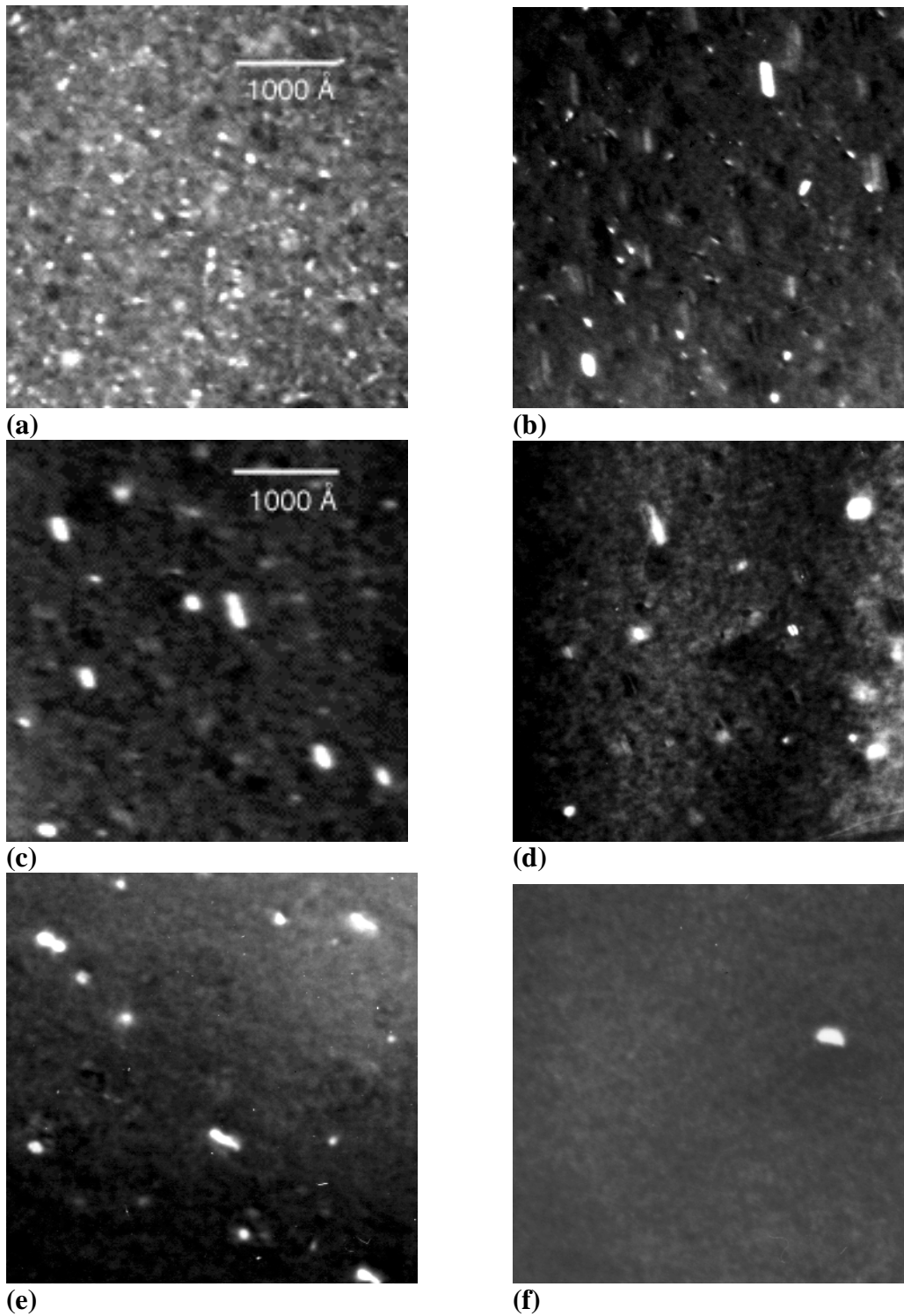


Figure 3.13 PTEM micrographs of the 10 keV  $\text{Ge}^+$ ,  $1 \times 10^{15} \text{ cm}^{-2} \text{ Ge}^+$  implant whose amorphous layer was polished to 80 Å and annealed at 750 °C for (a) 5 min, (b) 15 min, (c) 30 min, (d) 45 min, (e) 60 min, and (f) 360 min.

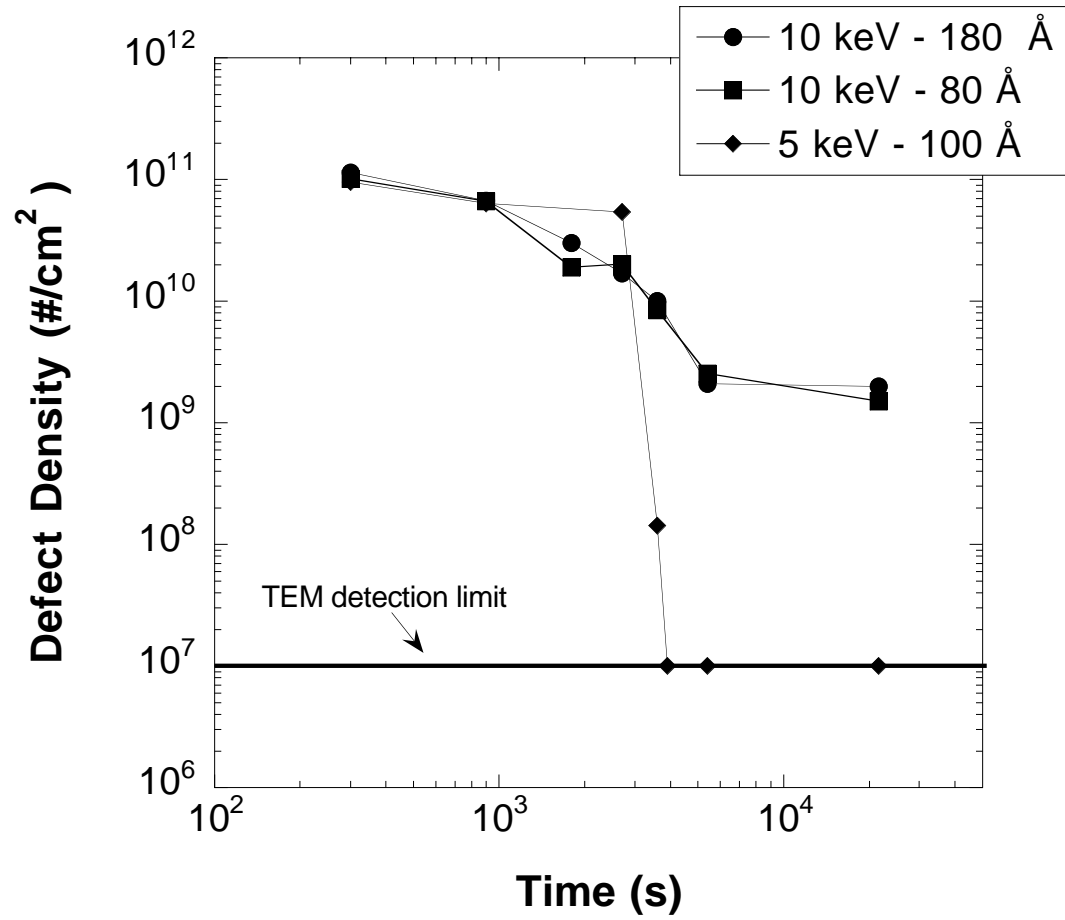


Figure 3.14 Defect evolution of the 5 keV, 10 keV, and 10 keV-lapped specimens annealed at 750 °C.

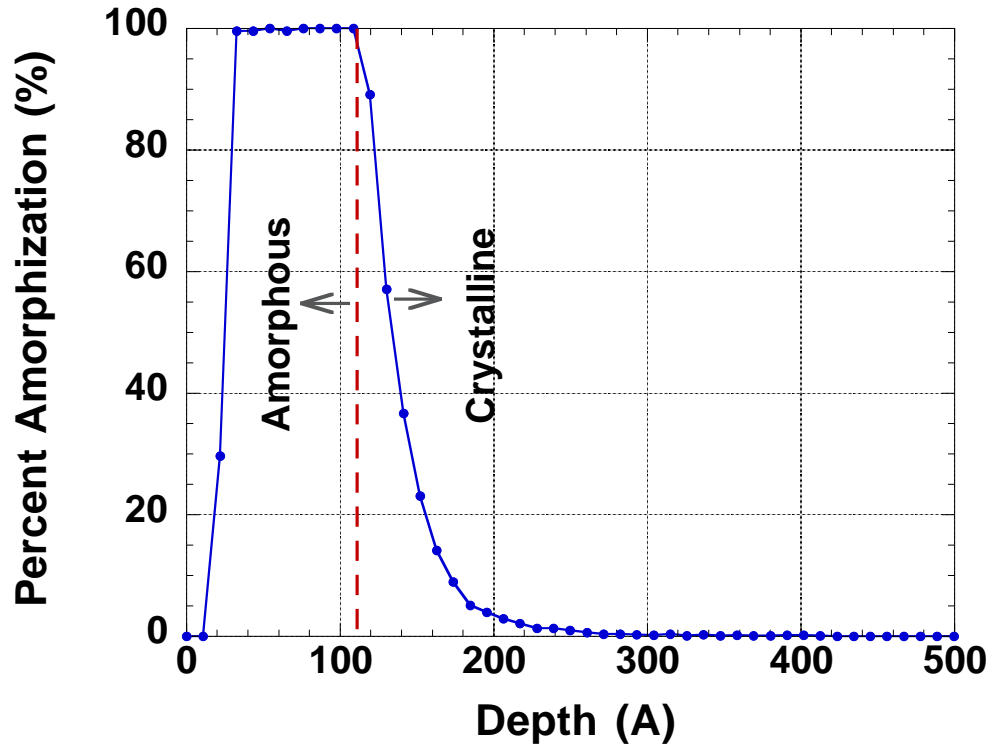


Figure 3.15 UT-Marlowe *.rbs* output for the 5 keV,  $1 \times 10^{15} \text{ Ge}^+ \text{ cm}^{-2}$  implant.

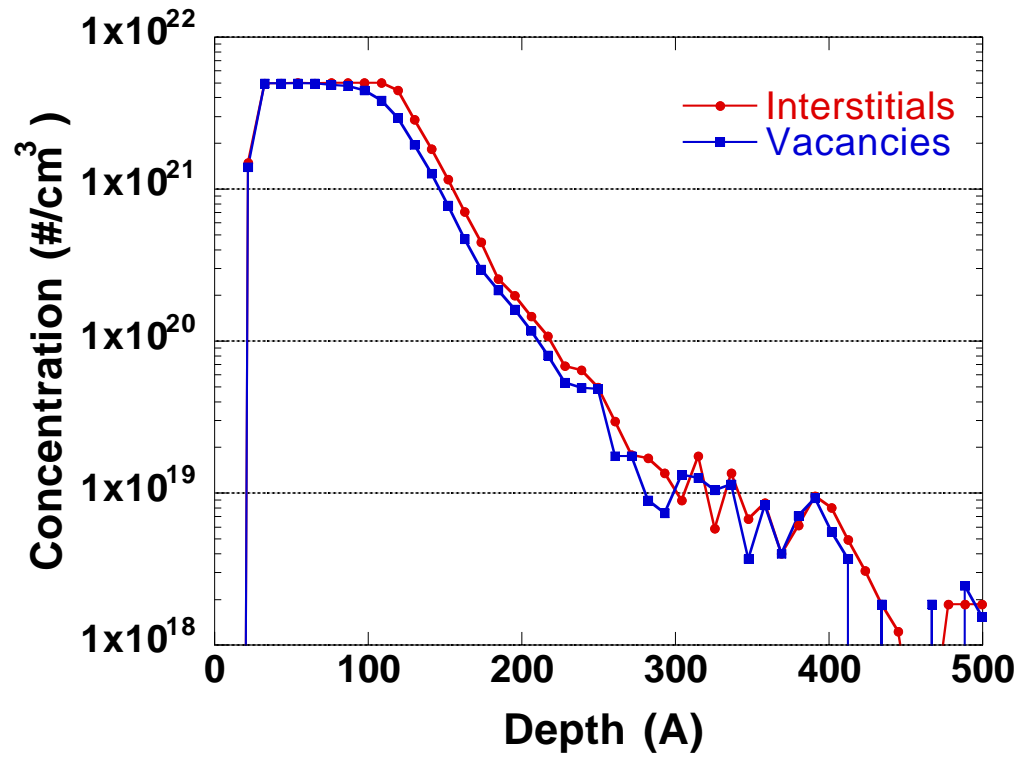


Figure 3.16 UT-Marlowe simulated interstitial and vacancy profiles for the 5 keV,  $1 \times 10^{15} \text{ Ge}^+ \text{ cm}^{-2}$  implant.

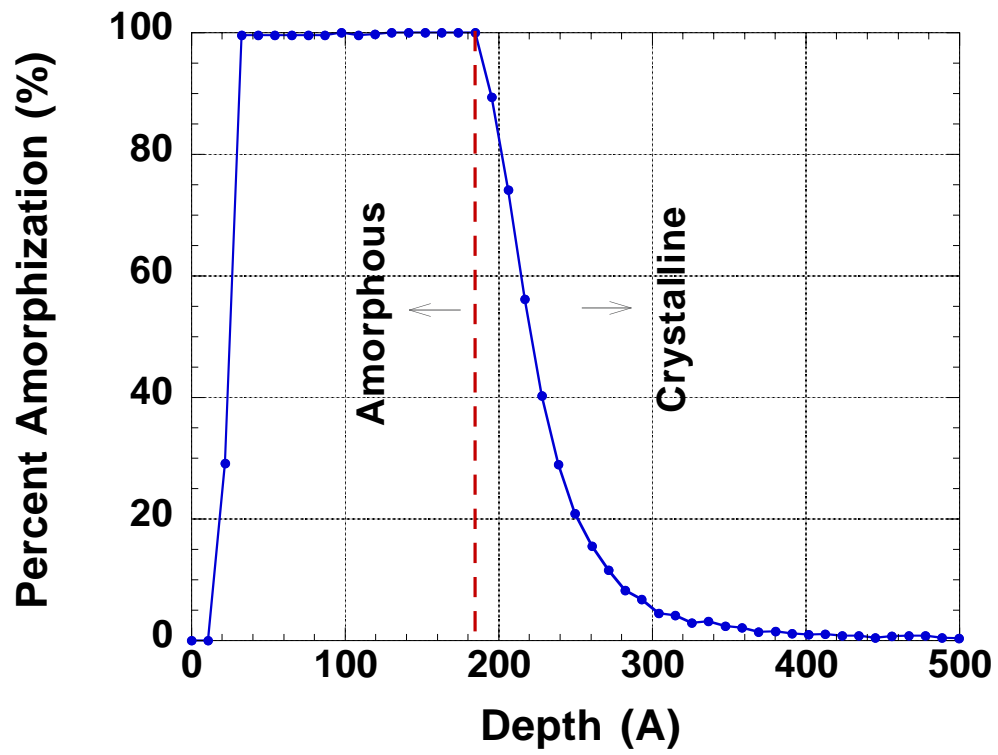


Figure 3.17 UT-Marlowe .rbs output for the 10 keV,  $1 \times 10^{15} \text{ Ge}^+ \text{ cm}^{-2}$  implant.

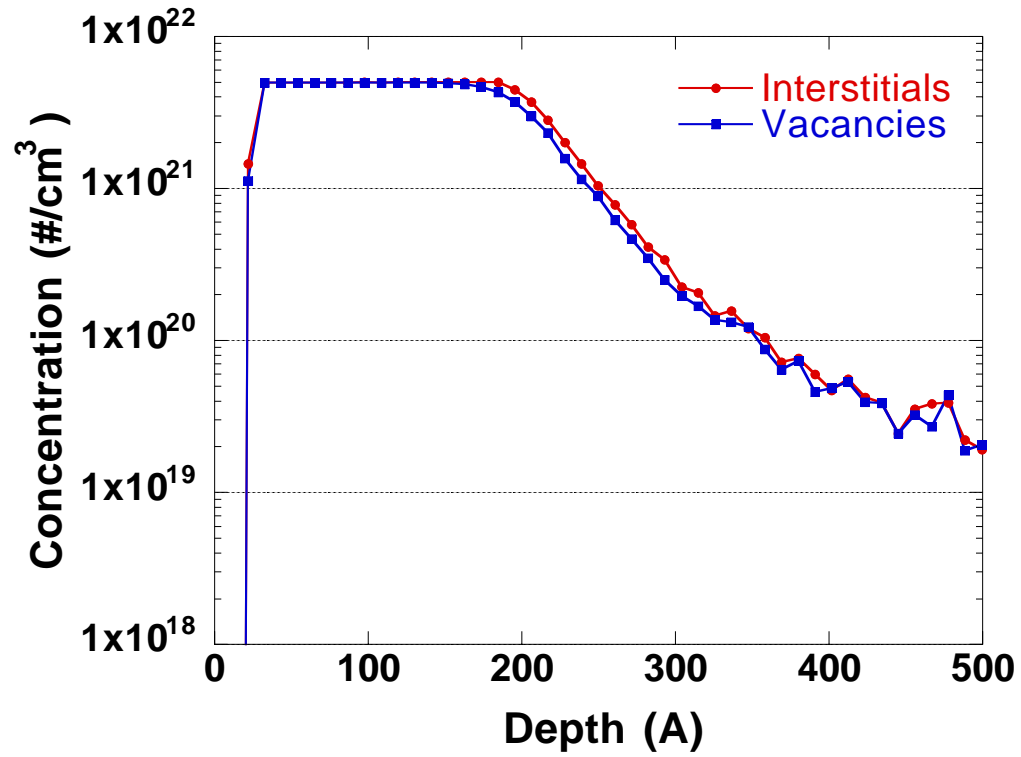


Figure 3.18 UT-Marlowe simulated interstitial and vacancy profiles for the 5 keV,  $1 \times 10^{15} \text{ Ge}^+ \text{ cm}^{-2}$  implant.

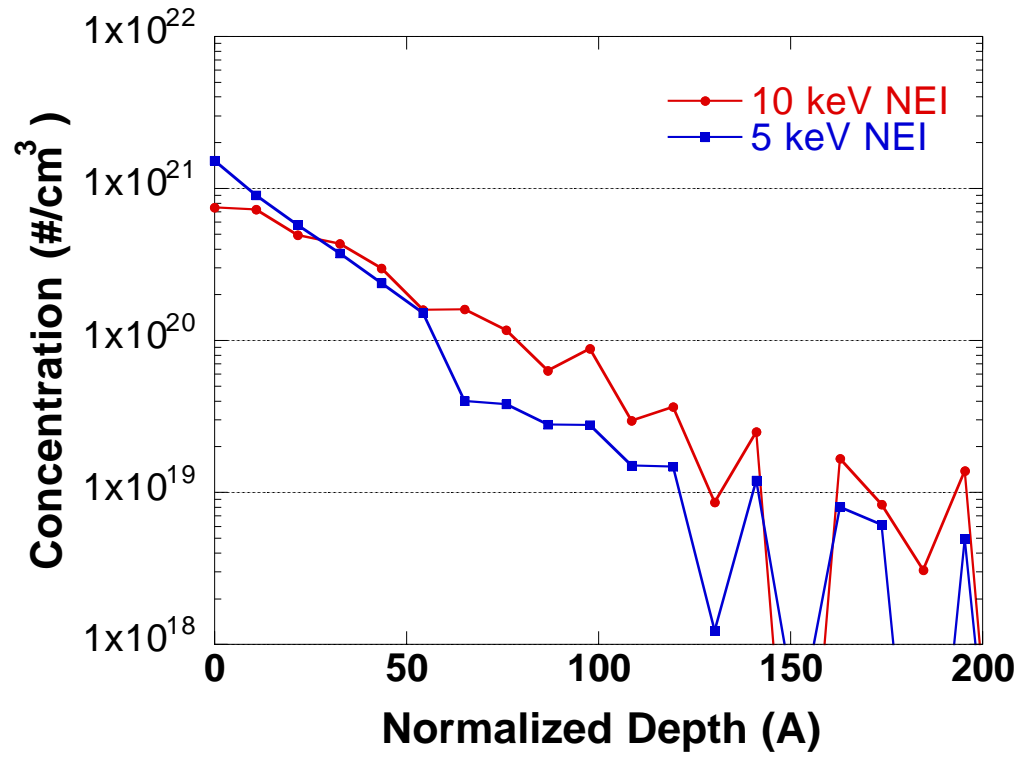


Figure 3.19 NEI profile for the 5 and 10 keV,  $1 \times 10^{15} \text{ Ge}^+ \text{ cm}^{-2}$  implants.

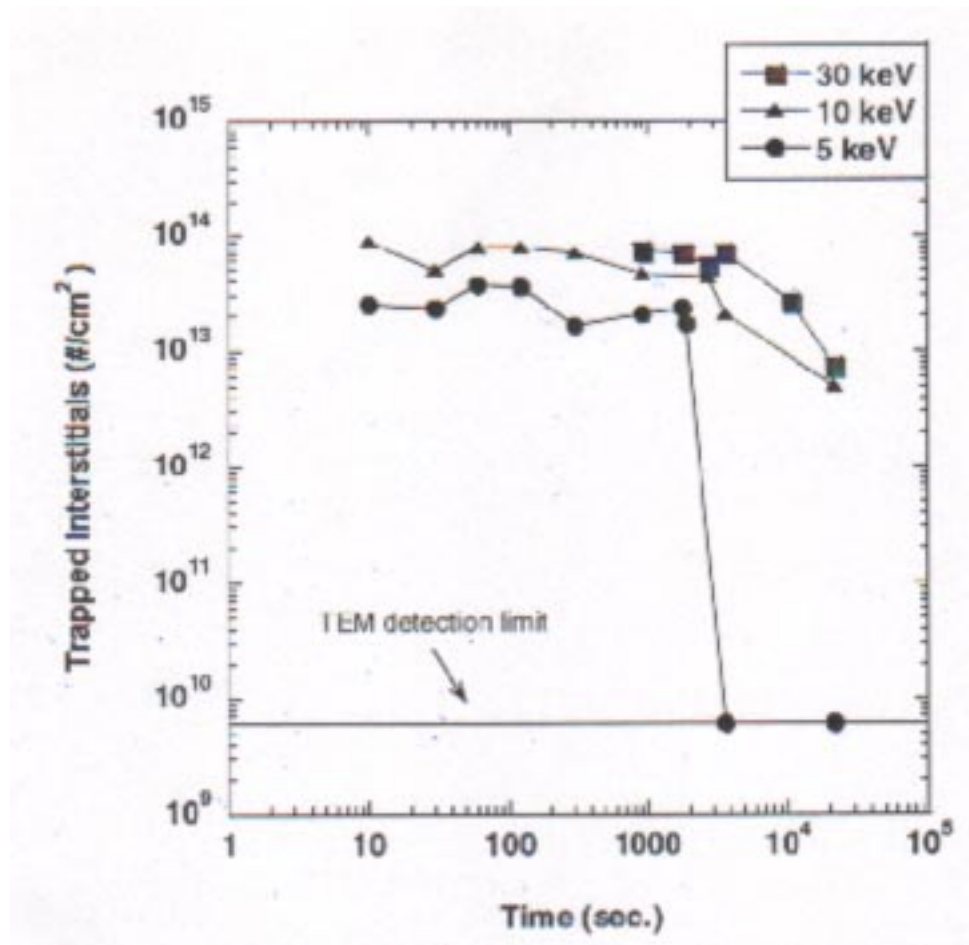


Figure 3.20 Trapped interstitial concentrations from 5, 10 and 30 keV,  $1 \times 10^{15} \text{ cm}^{-2} \text{ Ge}^+$  implants annealed at 750 °C, as reported by Gutierrez [42].

## CHAPTER 4 SURFACE PROXIMITY EXPERIMENT

### 4.1 Overview

In Chapter 3 an amorphous layer lapping experiment showed that increased surface proximity was not the key factor responsible for the defect dissolution observed in the 5 keV case. This finding again raises the argument of the role of the surface on excess interstitials. Does increasing the surface proximity to excess interstitials in the EOR region cause increased annihilation of these interstitials as proposed by Meekinson [47], Narayan [48], and Raman [49]? To approach this question from a low energy standpoint a 10 keV,  $1 \times 10^{15} \text{ Ge}^+ \text{ cm}^{-2}$  implant was used in a continuation of the amorphous layer lapping experiment from Chapter 3.

In this present experiment, the amorphous layer of a 10 keV implant was reduced to various depths and annealed at 750 °C for 15 and 45 min and the subsequent extended defects and trapped interstitial concentrations are studied using PTEM. By reducing the amorphous layer thickness, the EOR region and the excess interstitials that reside there are brought in closer proximity to the surface.

### 4.2 Experimental Results

The 10 keV implant forms a continuous amorphous layer 180 Å deep, as shown in Figure 3.11. The lapping procedure produced specimens with 155, 125, 80, and 40 Å. Figure 4.1 shows the XTEM images of the amorphous layer depths for the 155, 125, and

40 Å specimens. The 80 Å specimen is the same one from Chapter 3, and its XTEM image is also shown in Figure 3.11. Figure 4.2 shows PTEM micrographs of the 155, 125, and 40 Å specimens annealed at 750 °C for 15 and 45 min. The reader is referred to Figure 3.12 and 3.13 for the PTEM micrographs for the 180 Å and 80 Å specimens. The micrographs show that the defect population for the 155, 125, and 80 Å specimens are very similar to the control, 180 Å specimen. On the other hand, the 40 Å specimen's PTEM micrographs look a little different. There is a smaller population of small clusters or dislocation loops and no clear {311} defects are visible.

The defect densities and trapped interstitial concentrations for the five specimens are shown in Figure 4.3 and 4.4, respectively. The defect densities show no clear trend that can be correlated to increased surface proximity. The 155 and 125 Å specimens have higher defect density values than the 180 Å specimen after 15 min. However, after 45 min the 80 Å specimen is the only specimen with a higher defect density than the control. With the shallowest amorphous layer depth of 40 Å the smallest the smallest concentration of trapped interstitials exists at 15 min, but this trend is does not hold at 45 min. After 45 min, the 180 Å control specimen maintains the largest concentration of trapped interstitials, which may support that at longer annealing times increased surface proximity may be responsible for increased interstitial annihilation, but overall the defect densities and trapped interstitial concentrations are within the intrinsic 20 % error associated with this method of counting for all specimens and no clear effect of the surface can be determined.

Figures 4.5 and 4.6 show the defect densities separated by the defect type, dislocation loops and {311} defects, respectively. An important note here is that no clear

{311} morphology was observed in the 40 Å specimen PTEM micrographs, showing that at the shallowest amorphous layer depths {311} defects may not form. Figures 4.7 and 4.8 show the trapped interstitial concentrations separated by the defect type, dislocation loops and {311} defects, respectively. The average dislocation loops diameter is shown in Figure 4.9. It shows that there is a slight increase in defect diameter for 40 Å specimen, but it is within the error. The error bars reflect the standard deviation associated with the averaging of the diameters. Figure 4.10 shows the average defect length for the specimens, showing no clear trend.

### 4.3 Discussion

The overall trapped interstitial concentration with respect to amorphous layer depth is shown in Figure 4.11. It is clear in Figure 4.11 that there is no trend related to surface proximity on trapped interstitial concentration after 15 min of annealing time, until the shallowest depth of 40 Å when the amorphous layer depth approaches that of the average dislocation loop diameter. At the longer annealing time of 45 min, the trend does not hold further showing that the trapped interstitial population is independent of amorphous layer depth and therefore surface proximity.

The lapping experiment in Chapter 3, which only considered the 180 and 80 Å specimens quantified the defect evolution over 360 min of annealing time. At the longer annealing times, there was no evidence that the increased surface proximity, roughly half of the interstitials diffusion distance between the two specimens in this case, had any effect on the interstitial concentration. Figure 3.13 shows that after 360 min, large, stable dislocation loops are present in both specimens and Figure 3.14 shows that their defect densities are comparable throughout the annealing times. The totality of these findings

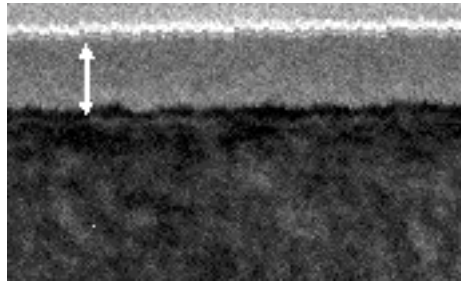
show that the model proposed by Omri [50] is still valid with amorphous layers very close to the surface, in that the surface does not have an effect on defect evolution of EOR damage.

These results also shed doubt on the concept of an image force exerted by the free surface onto dislocation loops as suggested by Narayan and Jagannagham [48]. In this theory the image force is proportional to the ratio of defect size divided by its distance to the surface ( $F \propto d/L$ ). Narayan and Jagannagham theorized that dislocation loops with diameters greater than  $2L$  will move to the surface and there will be a band of defect free crystal in that region. The results in this thesis show that dislocation loops exist very close to the surface and are not drawn to the surface by an image force.

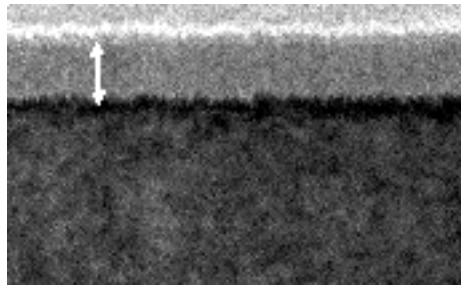
#### 4.4 Conclusion

In this chapter the amorphous layer of a 10 keV,  $1 \times 10^{15} \text{ Ge}^+ \text{ cm}^{-2}$  implant was lapped to thicknesses reduced from 180 Å to 165, 125, 80, and 40 Å. The specimens were then annealed at 750 °C for 15 and 45 min. The defect populations for the control-180 Å, 165, 125, and 80 Å specimens were all very similar to each other at both annealing times. However, the 40 Å specimen formed slightly larger dislocation loops and had a smaller interstitial population than the other specimens but was within the error of TEM analysis. After 45 min the control specimen had the highest concentration of trapped interstitials, which may be evident that the surface does have some effect after longer annealing times, but is not clear from the error.

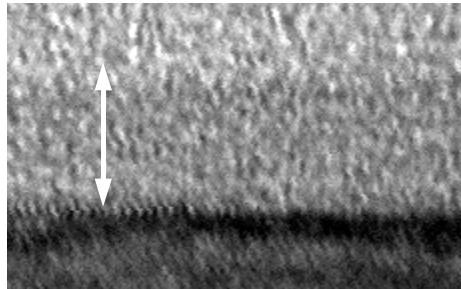
250 Å



(a)



(b)



(c)

Figure 4.1 XTEM images of 10 keV  $1 \times 10^{15} \text{ Ge}^+ \text{ cm}^{-2}$  specimens whose amorphous layers were lapped to (a) 155 Å, (b) 125 Å, and (c) 40 Å.

1000 Å

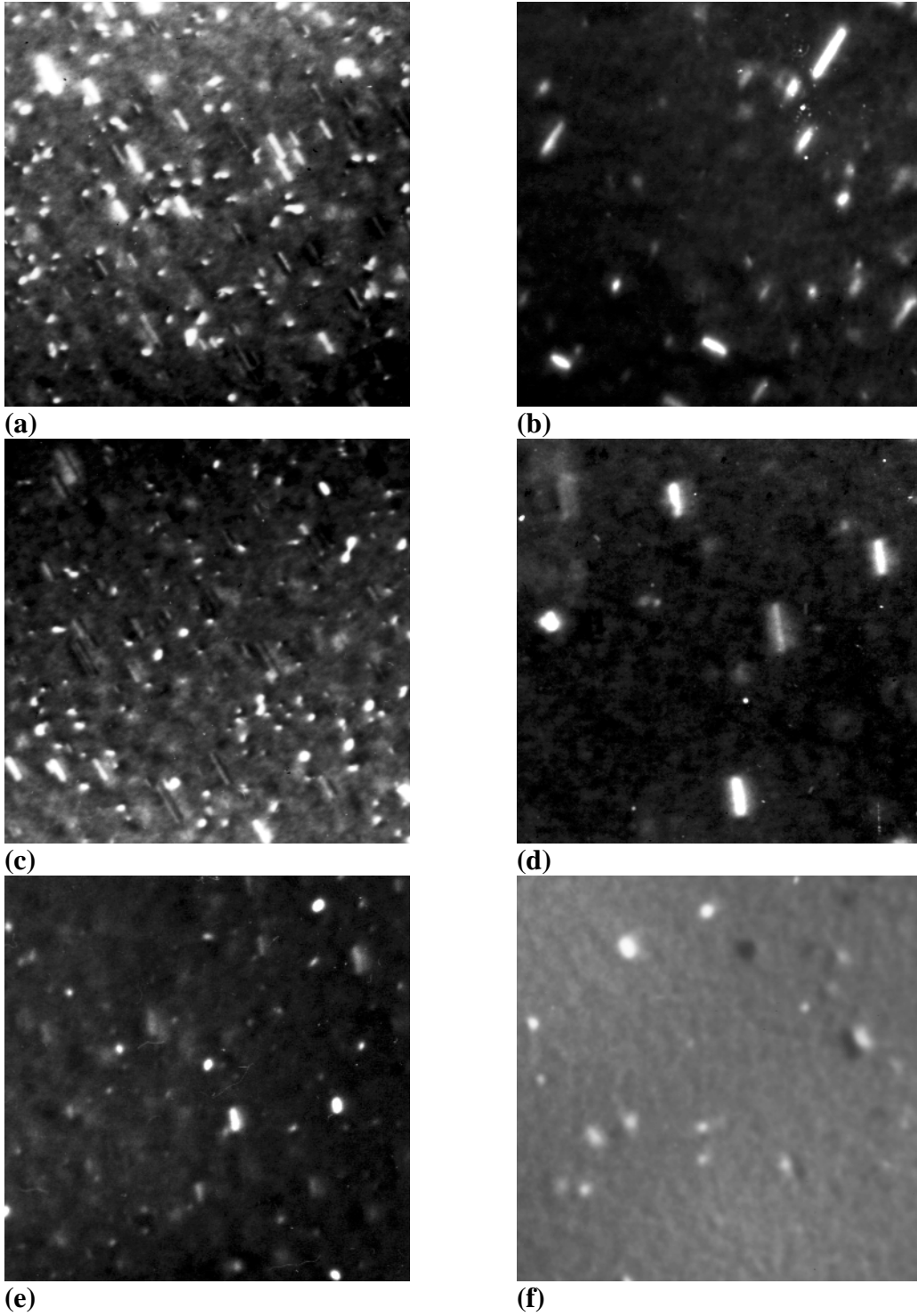


Figure 4.2 PTEM micrographs of the 155 Å specimen at (a) 15 and (b) 45 min, the 125 Å specimen at (c) 15 and (d) 45 min, and the 40 Å at (e) 15 min and (f) 45 min upon annealing at 750 °C.

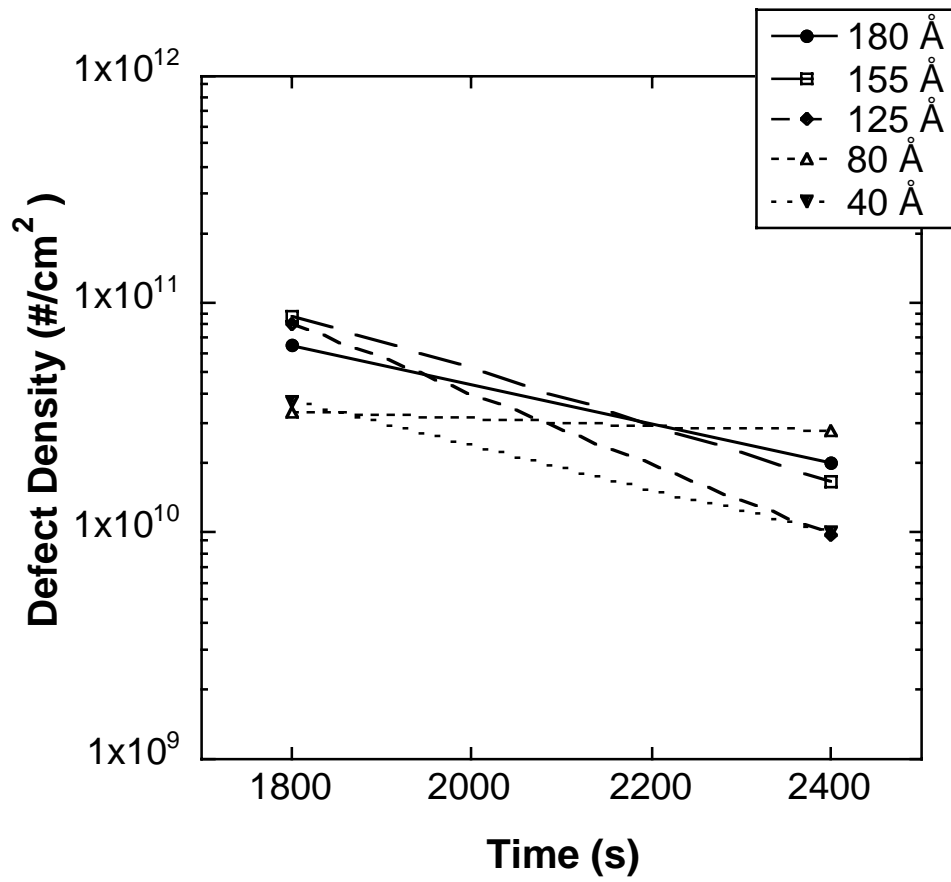


Figure 4.3 Defect densities for the 180, 155, 125, 80, and 40 Å specimens annealed at 750 °C.

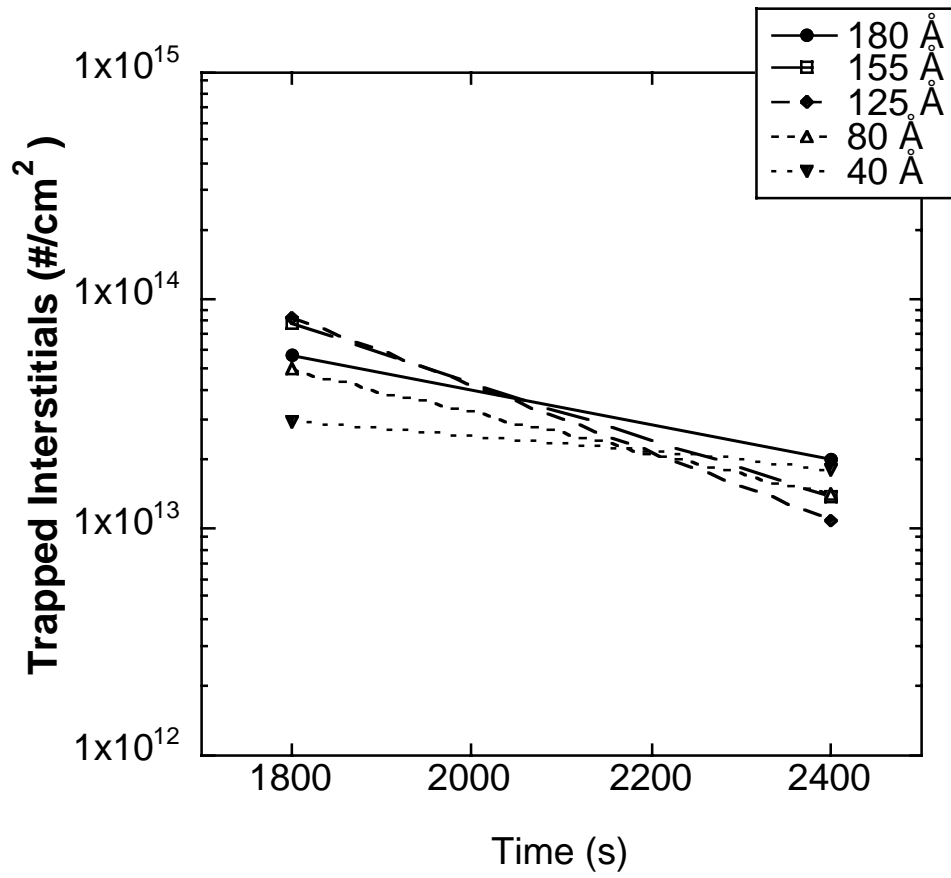


Figure 4.4 Trapped interstitial concentrations for the 180, 155, 125, 80, and 40  $\text{\AA}$  specimens annealed at 750  $^{\circ}\text{C}$ .

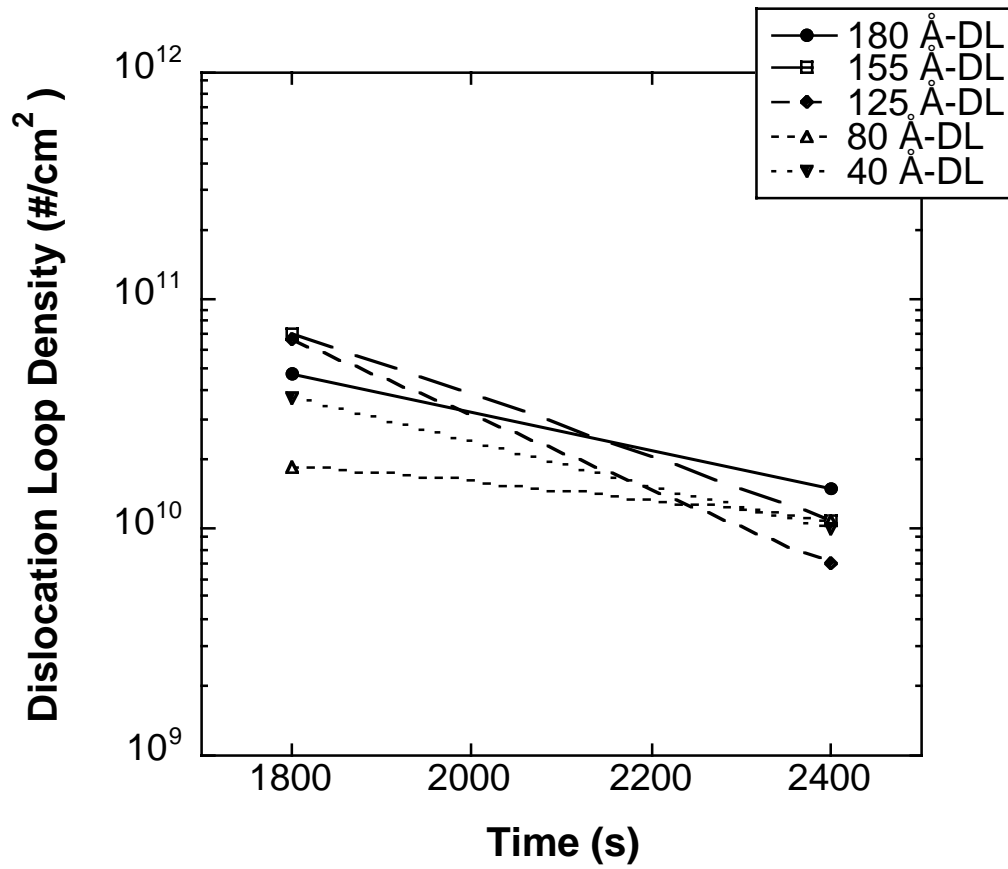


Figure 4.5 Dislocation loop component of the overall defect density for the 180, 155, 125, 80, and 40 Å specimens annealed at 750 °C.

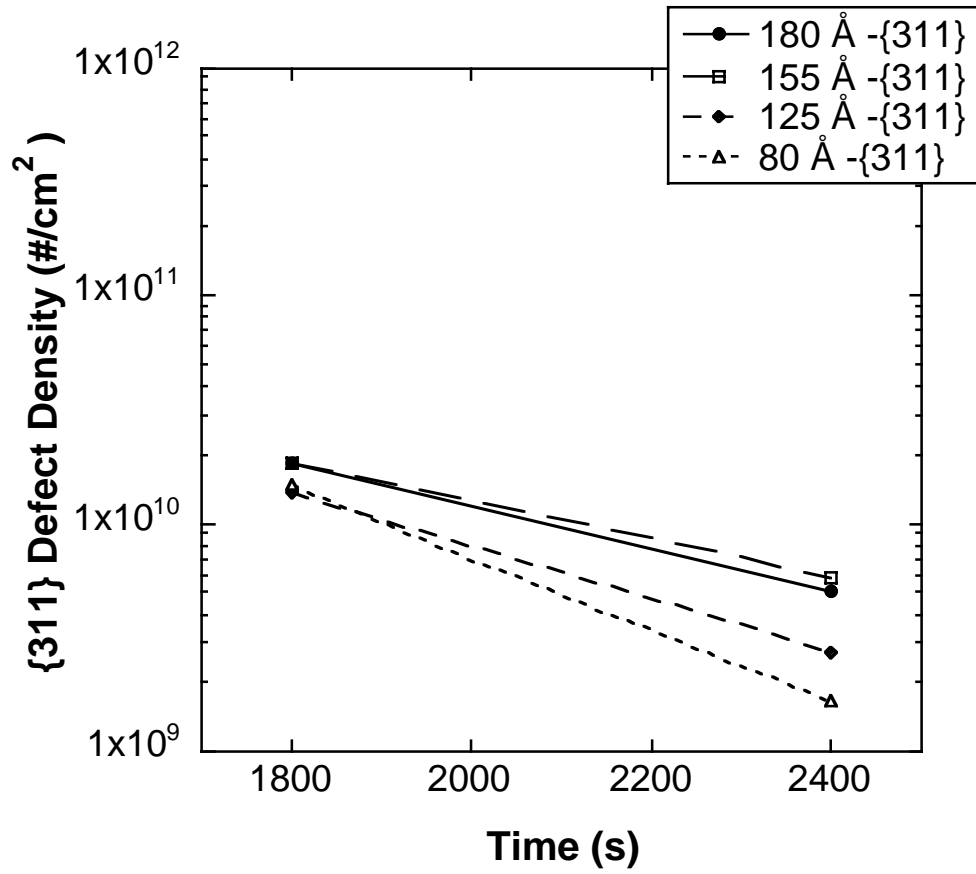


Figure 4.6 {311} defect component of the overall defect density for the 180, 155, 125, 80, and 40 Å specimens annealed at 750 °C.

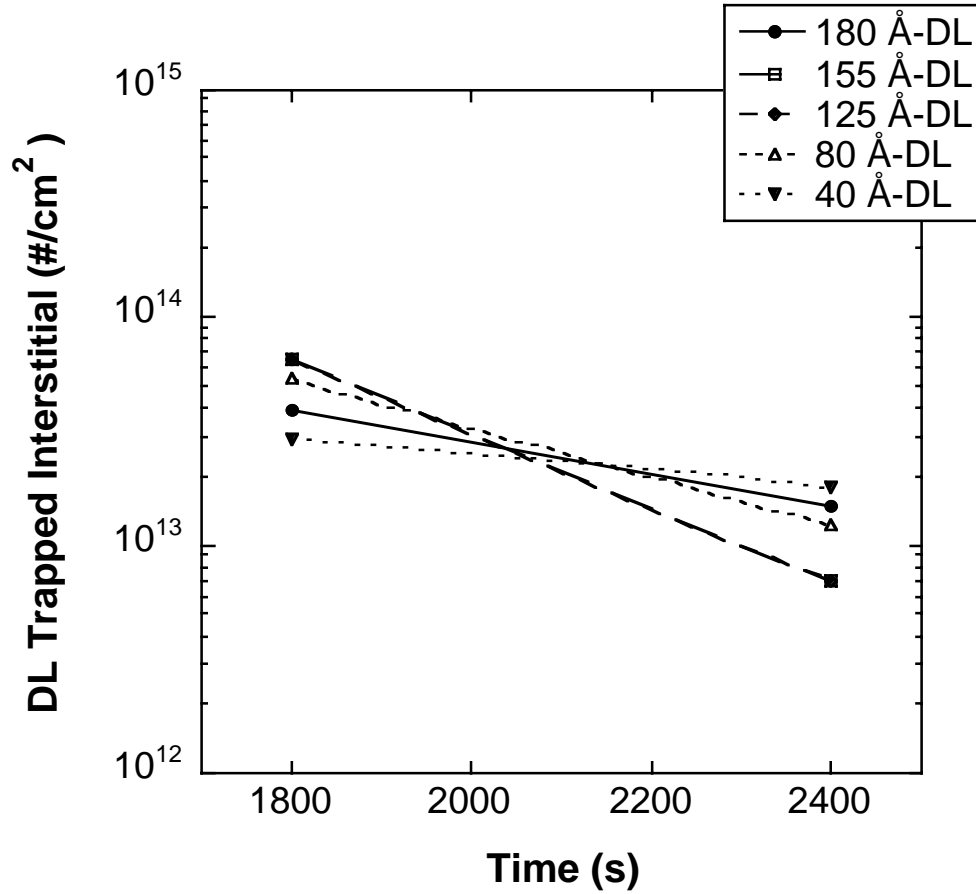


Figure 4.7 Dislocation loop component of the overall trapped interstitial concentration for the 180, 155, 125, 80, and 40  $\text{\AA}$  specimens annealed at 750  $^{\circ}\text{C}$ .

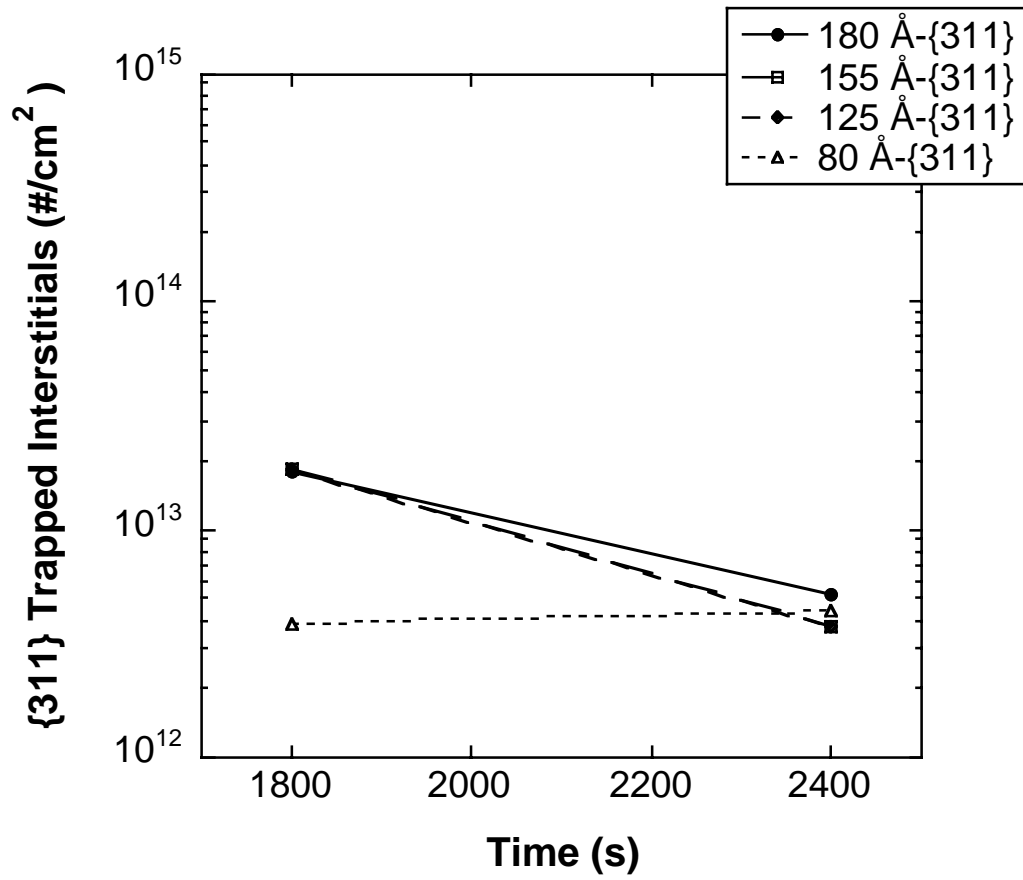


Figure 4.8 {311} defect component of the overall trapped interstitial concentration for the 180, 155, 125, 80, and 40 Å specimens annealed at 750 °C.

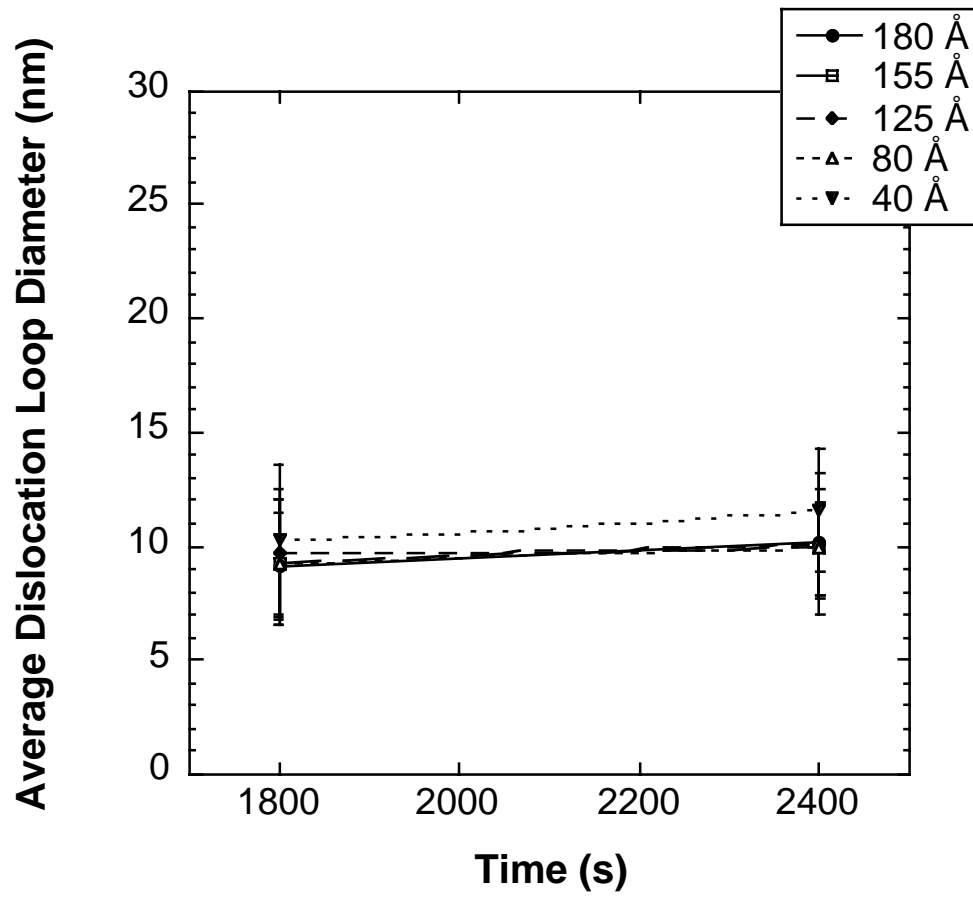


Figure 4.9 Average dislocation loop diameter for the 180, 155, 125, 80, and 40 Å specimens annealed at 750 °C.

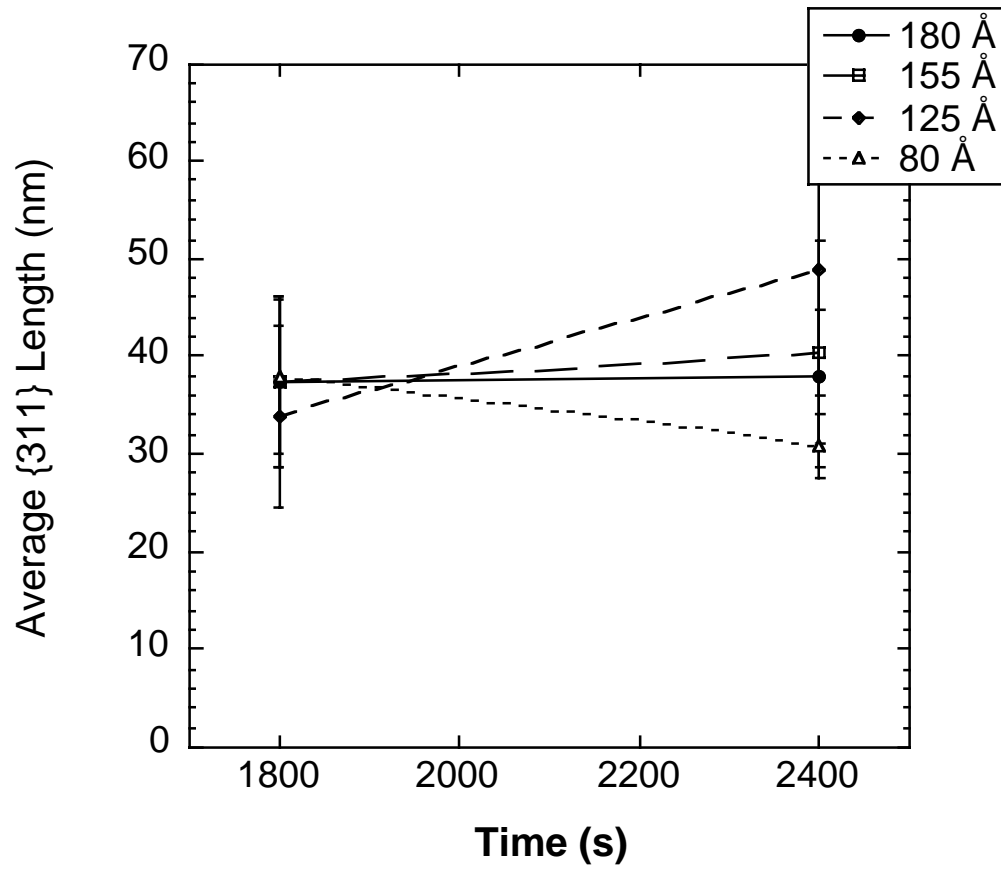


Figure 4.10 Average {311} defect length for the 180, 155, 125, 80, and 40 Å specimens annealed at 750 °C.

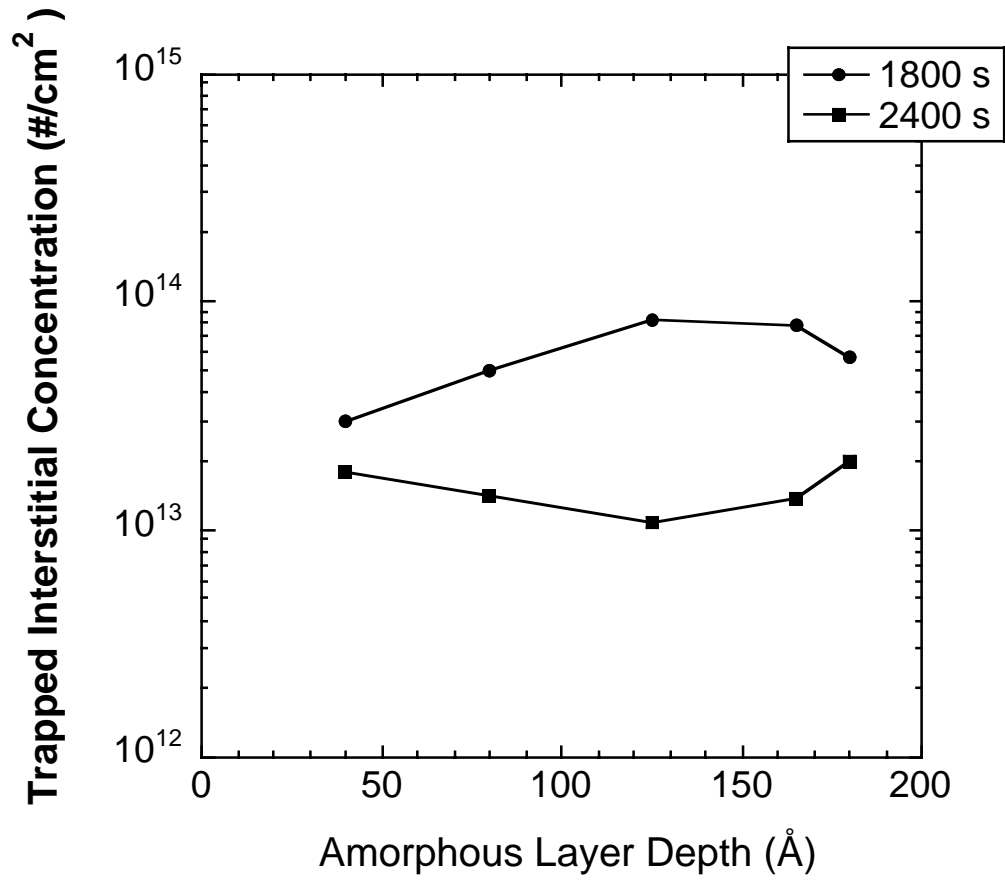


Figure 4.11 Trapped interstitial concentration with respect to amorphous layer depth for the 10 keV Ge<sup>+</sup> implant following a 750 °C anneal for 15 and 45 min.

## CHAPTER 5 LOW TEMPERATURE ANNEAL EFFECT ON ELLIPSOMETRY ACCURACY FOR SHALLOW AMORPHOUS SILICON LAYERS

### 5.1 Overview

As results show in the previous chapters of this thesis, ellipsometry measurements of shallow amorphous silicon layers are not very accurate when compared to high-resolution transmission electron microscopy (HRTEM) results. The roughness of the amorphous crystalline interface may be a factor which introduces error in the ellipsometry measurements. To test this hypothesis, silicon wafers with shallow amorphous layers were annealed at 400 °C for times ranging from 5 – 80 min in an attempt to smooth out the phase transition between the amorphous layer and the crystalline substrate. The efficacy of the low temperature anneal will be determined by comparing ellipsometry results at each annealing time to HRTEM results. The roughness of the amorphous/crystalline interface is then measured using HRTEM to correlate to the improved accuracy of the ellipsometry measurements.

### 5.2 Experimental Results

Figure 5.1 shows the ellipsometry results compared to HRTEM measurements for the range of annealing times at 400 °C. Ellipsometry measurements were performed at 0, 5, 10, 20, 40, 60, and 80 min, while HRTEM specimens were only imaged at 0, 40, and 80 min of annealing time. In the Figure 5.1 the average of three ellipsometry

measurements are plotted with error bars representing the standard deviation of the averages. However, the ellipsometry measurements are very precise with typical standard deviations in the measurements  $< 1.0 \text{ \AA}$  making the error bars indistinguishable in the figure.

The influence of the anneal is clearly shown to improve the accuracy of the ellipsometry measurements for the 5 and 10 keV case. For the 5 keV implant before the anneal, ellipsometry measured the amorphous layer depth to  $144 \text{ \AA}$ . After a 20 min anneal, the measured value changed to  $105 \text{ \AA}$ , an improvement of accuracy when compared to HRTEM of  $\sim 40\%$ . The same trend is shown with the 10 keV case. For the 30 keV case, the accuracy associated with the ellipsometry measurements was already good and did not improve over time. At  $400 \text{ }^\circ\text{C}$ , HRTEM showed no regrowth of the amorphous layer up to the longest anneal time of 80 min for any of the implant energy conditions.

The roughness of the amorphous/crystalline interface over the annealing time as measured by HRTEM is shown in Figure 5.2. The figure shows that roughness did decrease from the anneal, the mean peak-to-valley distance decreased. Figures 5.3 – 5.5 show HRTEM images of the amorphous layers for each implant energy. The images show that  $400 \text{ }^\circ\text{C}$  was too low to regrow the amorphous layer.

### 5.3 Conclusion

This experiment showed that the accuracy of ellipsometry measurements of shallow amorphous silicon layers on silicon substrates can be improved by decreasing the roughness of the amorphous/crystalline interface. At  $400 \text{ }^\circ\text{C}$ , the amorphous layer was shown not to regrow measurably at times ranging from 5 – 80 min. The implications of

this work may help researchers obtain more accurate amorphous silicon layer measurements using the quick, nondestructive technique of VASE.

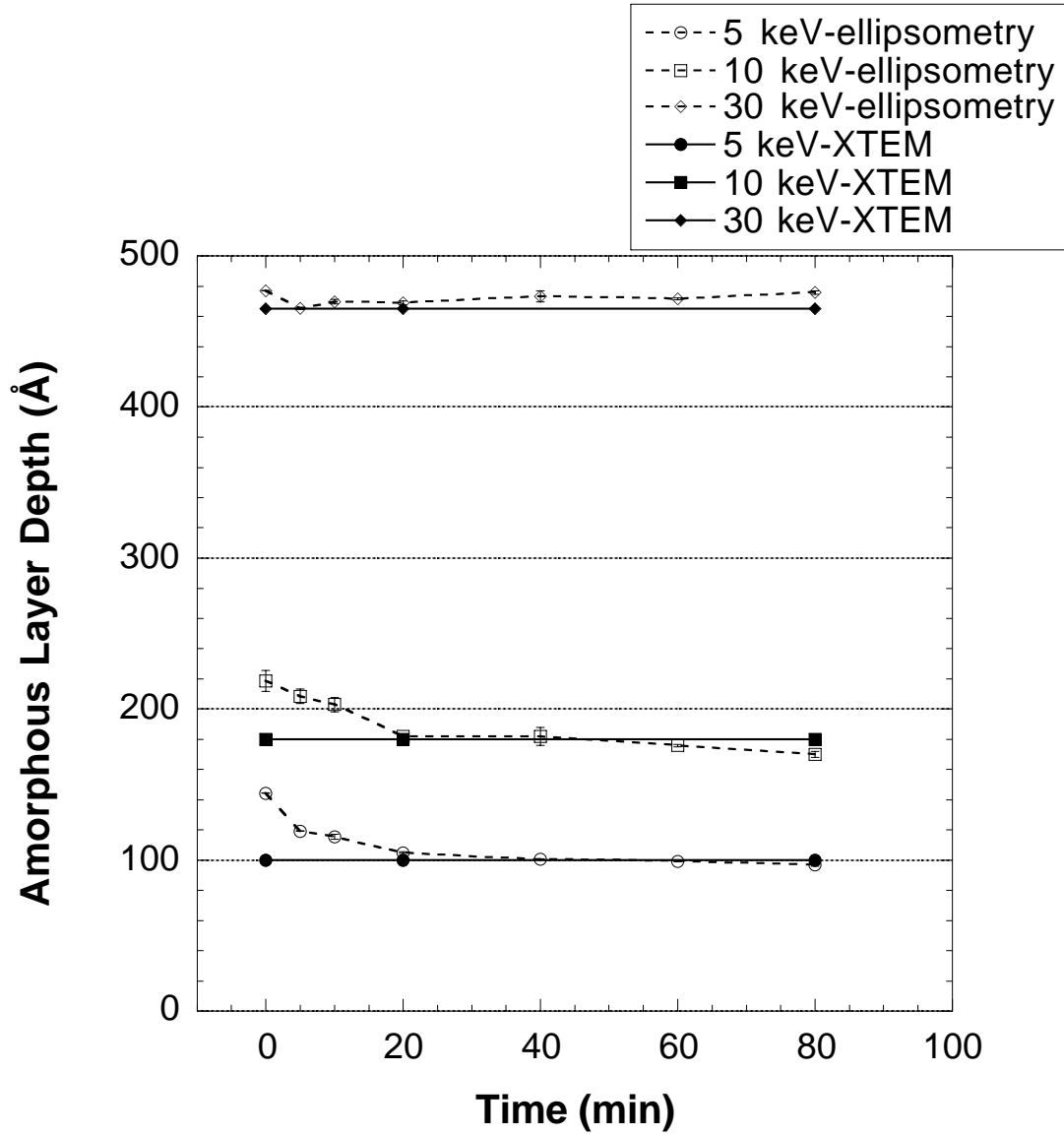


Figure 5.1 Comparison of amorphous layer depth measurements between ellipsometry and high resolution transmission electron microscopy following a 400 °C anneal over time.

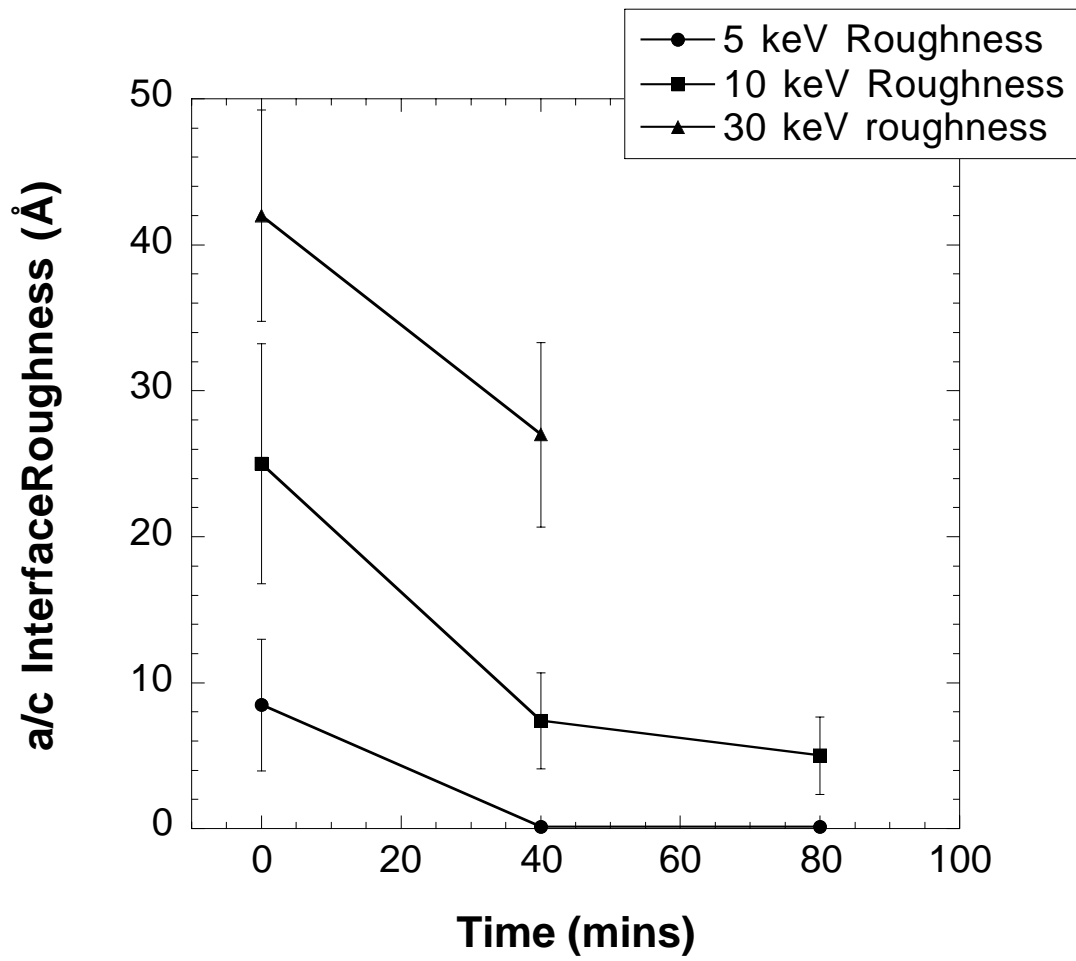
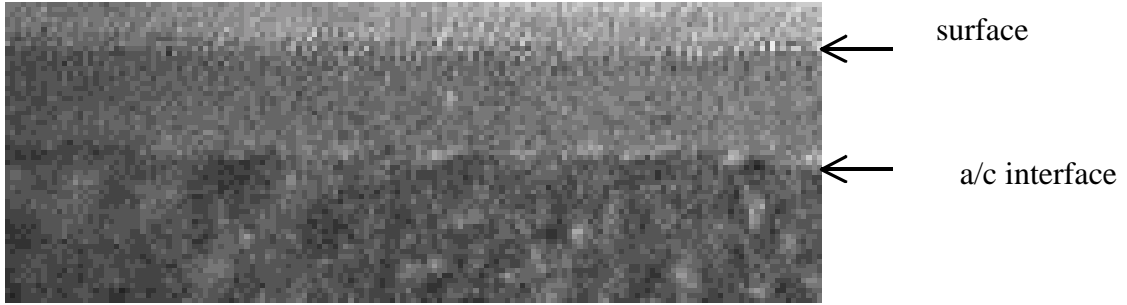


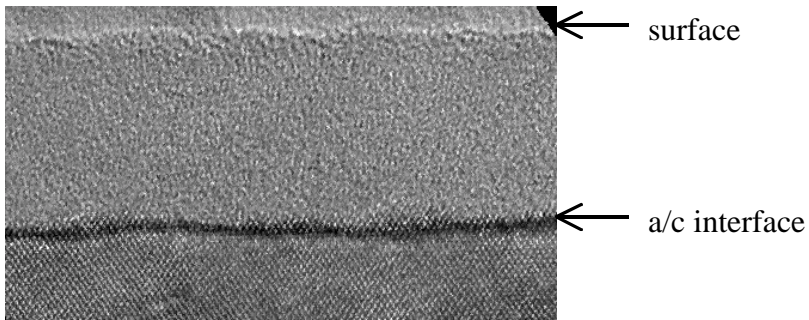
Figure 5.2 Reduction in amorphous/crystalline interface roughness as measured by high-resolution transmission electron microscopy following a 400 °C anneal.

100 Å



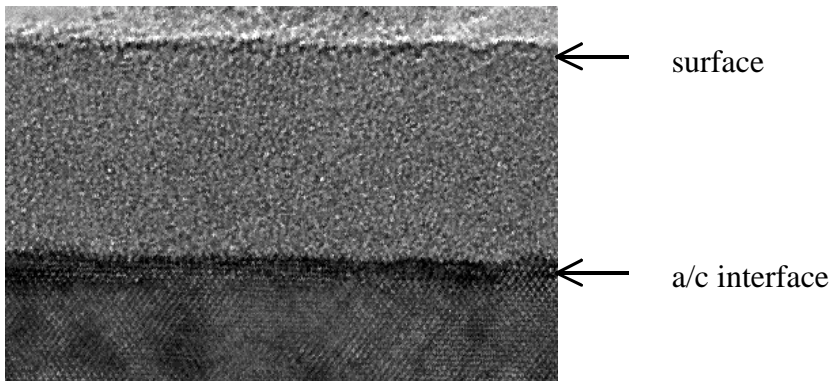
(a)

100 Å



(b)

100 Å



(c)

Figure 5.3 High-resolution transmission electron microscopy cross section images of 5 keV,  $1 \times 10^{15} \text{ Ge}^+ \text{ cm}^{-2}$  implant annealed at 400 °C for (a) 0 min, (b) 40 min, and (c) 80 min.

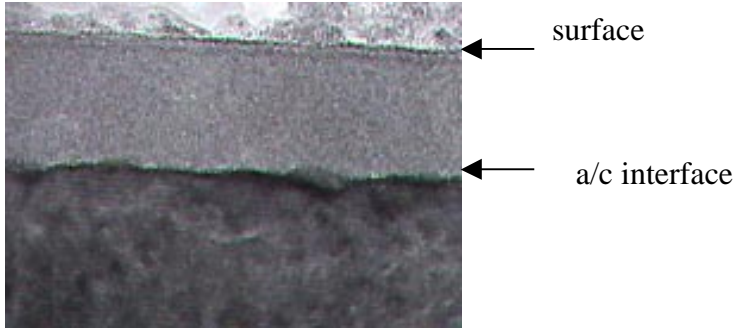
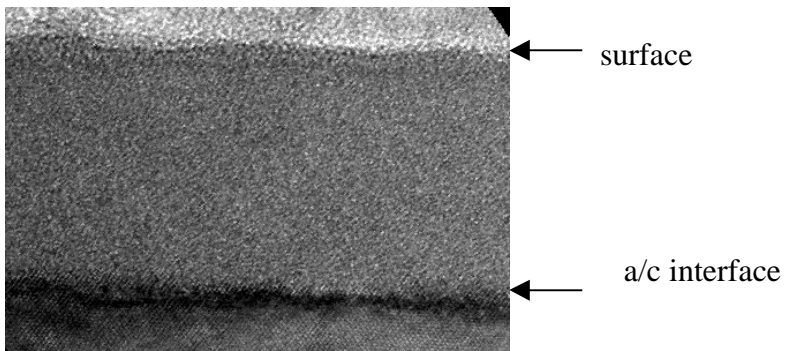
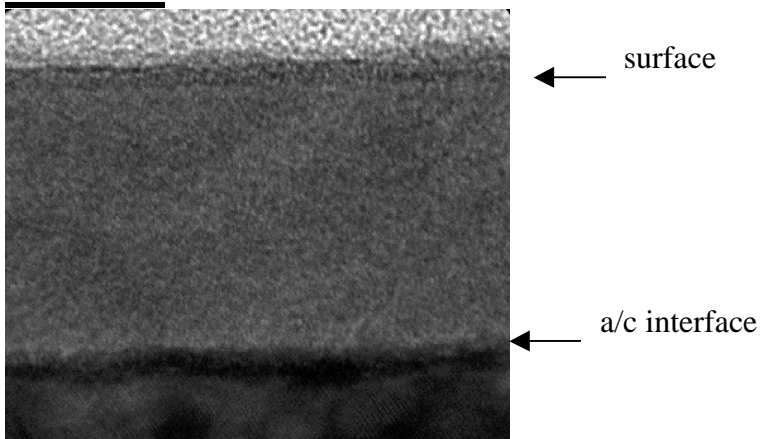
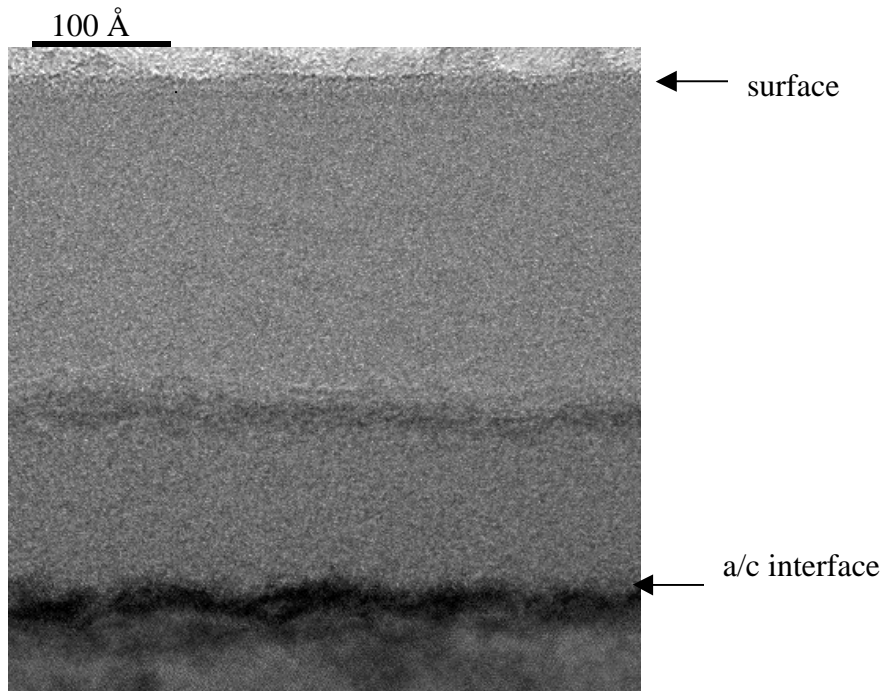
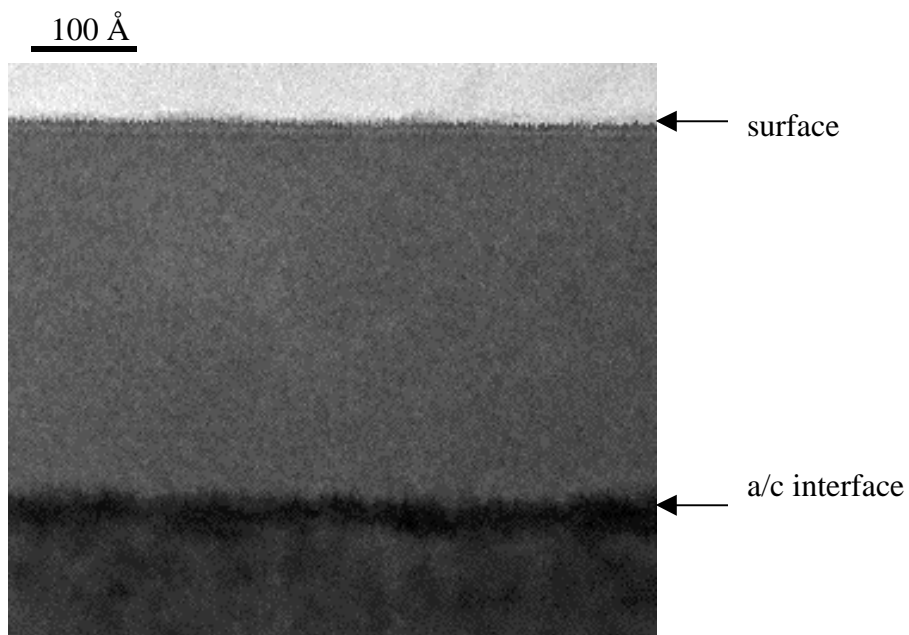
100 Å100 Å100 Å

Figure 5.4 High-resolution transmission electron microscopy cross section images of 10 keV,  $1 \times 10^{15} \text{ Ge}^+ \text{ cm}^{-2}$  implant annealed at 400 °C for (a) 0 min, (b) 40 min, and (c) 80 min.



(a)



(b)

Figure 5.5 High-resolution transmission electron microscopy cross section images of 30 keV,  $1 \times 10^{15} \text{ Ge}^+ \text{ cm}^{-2}$  implant annealed at 400 °C for (a) 0 min and (b) 40 min.

## CHAPTER 6 CONCLUSIONS AND FUTURE WORK

### **6.1 5 keV Ge<sup>+</sup> Defect Dissolution Study**

The small, unstable defects formed as a result of a 5 keV,  $1 \times 10^{15}$  Ge<sup>+</sup> cm<sup>-2</sup> implant into silicon were shown to have a dissolution activation energy of  $1.13 \pm 0.14$  eV, which is a value much less than the energies reported for dislocation loops (4.0 – 5.0 eV) [38] and {311} defects ( $3.8 \pm 0.02$  eV) [37]. The low activation energy may suggest that the defects dissolve by a glide process rather than a diffusion-controlled climb process. In the PTEM, the small defects show contrast consistent with dislocation loop morphology. However, these defects do not coarsen significantly like dislocation loops and dissolve very rapidly at high temperatures, as evident from the 1.13 eV activation energy.

It was shown that the 5 keV defect dissolution is strongly implant energy dependent. A lapping experiment reduced the amorphous layer of 10 keV implant, which forms {311} defects and later stable dislocation loops, to less than that of the 5 keV implant's amorphous layer and then the defect evolutions were compared. The 10 keV-lapped specimen's defect evolution strongly resembled that of the un-lapped 10 keV specimen, eliminating increased surface proximity as a possible explanation for the defect dissolution observed for the 5 keV energy. It is proposed that the 5 keV implant energy's small straggle and the low supersaturation of interstitials are responsible for forming this new defect morphology.

The results from this experiment have created as many if not more questions than they have answered. Possible future work in this area is needed to determine at what specific implant energy does the unstable dislocation loops form. This can be determined by obtaining implant of the same dose at energies between 5 and 10 keV and study the defect evolution. Another potential experiment is needed to determine the effect of germanium in the silicon on forming the defects, whether there is a strain or chemical influence.

In addition, the results may indicate that there is a lower supersaturation of interstitials in the EOR for the 5 keV case. An experiment that solves for the supersaturation of excess interstitials by measuring the diffusion enhancement of a buried boron marker would help determine if this was true. Another experiment that may warranted is to determine to defect dissolution activation energy for the dislocation loops observed in for the 10 keV case to see if they dissolve with the 4-5 eV activation energy, or if there is a step function decrease in the stability of defects as the implant energy is reduced. A final experiment that may be warranted is to see what effect the presence of boron may have on the defect evolution and what extent the dissolution, if any would have on TED and boron diffusion in general.

## **6.2 Surface Proximity Experiment**

This experiment lapped the amorphous layer of a 10 keV,  $1 \times 10^{15} \text{ Ge}^+ \text{ cm}^{-2}$  implant into silicon from 180 Å to depths of 165, 125, 80 and 40 Å for four different specimens. The defect population was analyzed following anneals at 750 °C for 15 and 45 min to determine if there is a measurable effect from increased proximity to the wafer's surface on excess interstitials in the EOR. It was determined that there is no clear

influence of the surface in the annihilation of interstitials for amorphous layers 80 Å or thicker. The specimen with a 40 Å thick amorphous layer showed a slight smaller defect and interstitial population than the thicker amorphous layer specimens at 15 min, but the trend did not hold after 45 min. This may suggest that there is somewhat of a surface effect at distances roughly equal to the radius of a dislocation loop.

### **6.3 Low Temperature Anneal Effect on Ellipsometry Accuracy for Shallow Amorphous Silicon Layers**

A low temperature anneal, at 400 °C, was shown to improve the accuracy of ellipsometry depth measurements for amorphous silicon layers on silicon substrates. Measurements were performed on 5, 10, and 30 keV Ge<sup>+</sup> implants all at a dose of  $1 \times 10^{15} \text{ cm}^{-2}$  with no anneal and then compared to samples that had been annealed for times from 5 – 80 min. The error in amorphous layer depths was reduced from about 40 % to practically 0% after 20 min of annealing time. High – resolution cross sectional transmission electron microscopy measured a reduction in the amorphous/crystalline interface roughness over time in the anneal, which was correlated to the improved accuracy of the ellipsometry measurements.

### **6.4 Implications of Findings**

The defects created by the 5 keV implant show that there is a different regime of damage associated with low energy, amorphizing implants that is not understood very well at this point. The simple assumption that the surface acts to reduce the excess interstitial supersaturation was shown to be invalid, or at least not significant. It is clear that more investigations are necessary to construct an accurate model of extended defect

evolution associated within this regime. This will assist the semiconductors industry in its drive to meet scaling requirements by more accurately predicting dopant diffusion profiles as the implant energy is also scaled.

## LIST OF REFERENCES

1. Plummer, J.D., M.D. Deal, and P.B. Griffin, *Silicon VLSI Technology*. 2000, Upper Saddle River, NJ: Prentice Hall. p. 11.
2. Moore, G.E., *Electronics*, 1965. **38**(8): p. 114 - 117.
3. SIA. *International Technology Roadmap for Semiconductor* (Semiconductor Industry Association, San Jose, Ca 2002). 2002.
4. Liu, T.M. and W.G. Oldham, *IEEE Elec. Dev. Lett.*, 1983. **EDL-4**: p. 59-62.
5. Ruggles, G.A., Hong, S. -N., Wortman, J. J., Ozturk, M., Myers, E.R., Hren, J. J., and Fair, R. B., MCNC, Technical Report, 1989. **TR89-04**.
6. Ozturk, M.C., Wortman, J. J., Osburn, C. M., Ajmera, A., Rozgonyi, G. A., Frey, E., Chu, W.-K., and Lee, C., *Trans. Elec. Dev.*, 1988. **35**: p. 659-667.
7. Simonton, R.B., *Nucl. Inst. and Meth. in Phys. Res. B*, 1987. **21**: p. 490-492.
8. Csepregi, L., Kennedy, E. F., Mayer, J. W., and Sigmon, T. W., *J. Appl. Phys.*, 1978. **49**(7): p. 3906.
9. Narayan, J., O.W. Holland, and B.R. Appleton, *J. of Vac. Sci. and Tech.*, 1983. **B 1**: p. 871.
10. Lindfors, C., Ph. D. Dissertaion, Department of Materials Science and Engineering. 2003, University of Florida: Gainesville, FL.
11. Hong, S.-N., Ruggles, G. A., Wortman, J. J., and Ozturk, M. C., *IEEE Trans. on Elect. Dev.*, 1991. **38**: p. 476-486.
12. Claverie, A., Laanab, L, Bonafos, C., Bergaud, C., Martinez, A., and Mathiot, D., *Nucl. Instr. and Meth. in Phys. Res. B*, 1995. **96**: p. 202-209.
13. Borland, J.O. *Low Temperature Shallow Junction Formation for 70nm Technology Node and Beyond*. in *Materials Research Society Symposium*. 2002, Warrendale, PA: Materials Research Society.
14. Talwar, S., Felch, S., Downey, D., and Wang, Yun., *IEEE Electr. Dev. Lett.*, 2000: p. 175-177.

15. McCoy, S.P., Gelpy, J., Elliot, K., Gable, K. A., Jain, A., and Robertson, L. S., 7th Int. Conf. on USJ, 2003: p. 104.
16. Current, M.I., *Ion Implantation for Bipolar-CMOS Device Fabrication*, in *Ion Implantation for Bipolar-CMOS Device Fabrication*, M.I. Current, Editor. 1997, Yorktown, NY: Ion Beam Press.
17. Mazzone, A.M., Phys. Stat. Sol. (A), 1989: p. 149.
18. Gyulai, J., K.S. Jones, and P. Petrik, *Radiation Damage and Annealing in Silicon*, in *Ion Implantation Science and Technology*, J.F. Ziegler, Editor. 2000, Ion Implantation Technology Co.: Yorktown, NY. p. 245.
19. Giles, M.D., J. of the Electro. Soc., 1991. **138**: p. 1160-1165.
20. Eaglesham, D.J., Stolk, P. A., Gossmann, H.-J., Haynes, T. E., and Poate, J. M., Nucl. Instr. and Meth. in Phys. Res. B, 1995. **106**: p. 191.
21. Pelaz, L., Gilmer, G. H., Jaraiz, M., Herner, S. B., Gossmann, H.-J., et al., Appl. Phys. Lett., 1998. **73**: p. 1421.
22. Holland, O.W., S.J. Pennycook, and G.L. Albert, Appl. Phys. Lett., 1989. **55**(24): p. 2503-2505.
23. Clark, M.H., M.S. Thesis, Department of Materials Science and Engineering. 2001, University of Florida: Gainesville, FL.
24. Williams, J.S., Nucl. Instr. and Meth. in Phys. Res. B, 1983. **209/210**: p. 219.
25. Poate, J.M. and J.S. Williams, in *Ion Implantation and Beam Processing*, J.S. Williams and J.M. Poate, Editors. 1984, Academic Press: New York, NY. p. 27.
26. Csepregi, L., L. Mayer, and T.W. Sigmon, Phys. Lett., 1975. **54A**: p. 157.
27. Licoppe, C. and Y.I. Nissim, J. Appl. Phys., 1986. **59**(2): p. 432-438.
28. Olson, G.L., Mat. Res. Soc. Symp. Proc, 1985. **35**: p. 25.
29. Jones, K.S., Ph.D. Dissertation, Department of Materials Science and Minerals Engineering. 1987, University of California at Berkeley: Berkeley. p. 133.
30. Jones, K.S., S. Prussin, and E.R. Weber, Appl. Phys. A, 1988. **45**: p. 1-34.
31. Prussin, S. and K.S. Jones, J. of the Electro. Soc., 1990. **137**: p. 1912-1914.
32. Mauduit, B.D., Lanaab, L., Berguard, C., Faye, M., Martinez A., and Claverie, A., Nucl. Instr. and Meth. in Phys. Res. B, 1994. **84**: p. 190-194.

33. Robertson, L.S., Jones, K. S., Rubin, L. M., and Jackson, J., J. Appl. Phys., 2000. **87**: p. 2910-2913.
34. Jones, K.S., "Annealing Kinetics of Ion Implanted Damage in Silicon," (Presentation, University of Florida, 2001).
35. Li, J. and K.S. Jones, J. Appl. Phys., 1998. **85**: p. 8137-8144.
36. Eaglesham, D.J., Stolk, P. A., Gossmann, H.-J., Haynes, T. E., and Poate, J. M., Appl. Phys. Lett., 1994. **65**(18): p. 2305-2307.
37. Stolk, P.A., Gossmann, H.-J., Eaglesham, D. J., Jacobson, D. C., Rafferty, C. S., Gilmer, G. H., et al., J. Appl. Phys., 1997. **81**(9): p. 6031-6049.
38. Siedel, T.E., Lischer, C. S., Pai, R. V., Knoell, D. M., and Jacobson, D. C., Nucl. Inst. and Meth. in Phys. Res. B, 1985. **7/8**: p. 251.
39. Lampin, E., V. Senez, and A. Claverie, J. Appl. Phys., 1999. **85**: p. 8137-8144.
40. Liu, J., M.E. Law, and K.S. Jones, Solid-State Electr. 1995. **38**: p. 1305-1312.
41. Bonafos, C., D. Mathiot, and A. Claverie, J. Appl. Phys., 1998. **83**: p. 3008-3017.
42. Gutierrez, A.F., M.S. Thesis, Department of Materials Science and Engineering. 2001, University of Florida: Gainesville.
43. Eaglesham, D.J., Agarwal, A., Haynes, T. E., Gossmann, H.-J., Jacobson, D. C., and Poate, J. M., Nucl. Inst. and Meth. in Phys. Res. B, 1996. **120**: p. 1-4.
44. Jain, S.C., Schoenmaker, W., Lindsay, R., Stolk, P. A., Decoutere, S., willander, M., and Mass, H. E., Appl. Phys. Rev., 2002. **91**(11): p. 8919-8941.
45. Jones, K.S., Zhang, L. H., Krishamoorthy, V., Law, M. E., Simmons, P., Chi, P., Rubin, L., and Elliman, Appl. Phys. Lett., 1996. **68**: p. 2672-2674.
46. Robertson, L.S., Law, M. E., Jones, K. S., Rubin, L., Jackson, J., Chi, P., and simons, D. S., Appl. Phys. Lett., 1999. **75**: p. 3844-3846.
47. Meekinson, C.D., Institute of Physics Conference Series, 1991. **117**: p. 197.
48. Narayan, J. and K. Jagannadham, J. Appl. Phys., 1987. **62**: p. 1694.
49. Raman, R., Law, M. E., Krishnamoorthy, V., and Jones, K. S., Applied Physics Letters, 1999. **74**(11): p. 1591-1593.
50. Omri, M., Bonofos, C., Claverie, A., Nejim, A., Cristiano, F., Alquier, D., Martinez, A., and Cowern, N. E. B., Nulc. Instr. and Meth. in Phys. Res. B, 1996. **120**: p. 5-8.

51. Ganin, E. and A. Marwick, Mat. Res. Soc., 1989. **147**: p. 13-18.
52. Williams, D.B. and C.B. Carter, *Transmission Electron Microscopy*. 1st ed. Vol. 3. 1996, New York: Plenum Press. p. 8.
53. Law, M.E., *Florida Object Oriented Process Simulator*. 1999, Gainesville, FL: University of Florida.
54. Bharatan, S., Ph.D. Dissertation, Department of Materials Science and Engineering. 1999, University of Florida: Gainesville, FL.
55. Obradovic, B., Wang, G., Chen, Y. Li, D., Snell, C., and Tasch, A. F. , *UT-Marlowe 5.0*. 1999, University of Texas, Austin; Los Alamos National Laboratory.
56. Li, J.-H., Law, M. E., Jasper, C., and Jones, K. S., Mat. Sci. in Semi. Proc., 1998. **1**: p. 99-106.
57. Herner, S.B., Gila, B. P., Jones, K. S., Gossmann, H.-J., Poate, J. M., and Luftman, H. S., J. of Vac. Sci. and Tech. B, 1996. **14**: p. 3593.
58. Edington, J.W., *The Operation and Calibration of the Electron Microscope*. 1974, Gloeilampenfabrieken: Philips.
59. Desmond, F.J., Kalbitzer S., Mannsperger H., and Damjantschitsch, H., Phys. Lett. **93A**, 503 (1983).
60. Frank, W., Gosele, U., Mehrer H., and Seger A., *Diffusion in Crystalline Solids*. 1984, New York: Academic Press.

## BIOGRAPHICAL SKETCH

I was born in 1978 on a U.S. Army base in Heidelberg, Germany. After graduating from Oviedo High School in Oviedo, FL, in 1997, I attended the University of Florida receiving my B.S. in materials science and engineering in May 2002. During my undergraduate coursework I played for the University of Florida lacrosse club team and interned with Texas Instruments in Dallas, TX, for seven months in 2000. In the fall of 2002 I began my graduate studies at the University of Florida in the SAWMP Group. After graduation I plan to obtain a rewarding engineering position.